The cryoEM structure of the *Hendra henipavirus* nucleoprotein reveals insights into paramyxoviral nucleocapsid architectures

Tim C Passchier[1Ψ], Joshua B R White[1], Daniel P Maskell[1], Matthew J Byrne[1], Neil A Ranson[1], Thomas A Edwards[1*#], John N Barr[1*]

[1]Astbury Centre for Structural Molecular Biology, School of Molecular and Cellular Biology, Faculty of Biological Sciences, University of Leeds, Leeds, LS2 9JT, United Kingdom

[Ψ]Current address: Department of Biology, University of York, York, YO10 5DD, UK

[#]Current address: Larkin University, College of Biomedical Sciences, 18301 N Miami Avenue, Miami, FL 33169 USA

*Corresponding authors: Thomas A Edwards (t.a.edwards@leeds.ac.uk); John N Barr (j.n.barr@leeds.ac.uk)

Abstract

We report the first cryoEM structure of the *Hendra henipavirus* nucleoprotein in complex with RNA, at 3.5 Å resolution, derived from single particle analysis of homotetradecameric RNA-bound N protein rings exhibiting D14 symmetry. The structure of the HeV N protein adopts the common bi-lobed paramyxoviral N protein fold; the N-terminal and C-terminal globular domains are bisected by an RNA binding cleft containing six RNA nucleotides and are flanked by the N-terminal and C-terminal arms, respectively. In common with other paramyxoviral nucleocapsids, the lateral interface between adjacent N and N_{+1} protomers involves electrostatic and hydrophobic interactions mediated primarily through the N-terminal arm and globular domains with minor contribution from the C-terminal arm. However, the HeV N multimeric assembly uniquely identifies an additional interaction between N_{+1} and N_{-1} protomers. The model presented here broadens the understanding of RNA-bound paramyxoviral nucleocapsid architectures and provides a platform for further insight into the molecular biology of HeV, as well as the development of antiviral interventions.

46 **Introduction**

47 The non-segmented, negative-sense RNA virus *Hendra henipavirus* (HeV) emerged in 1994 as
48 a fatal infectious agent on the Hendra racetracks of Brisbane, Australia, leading to the deaths of 15
49 horses and one human [1,2]. Since its discovery, there have been over 65 recognised and suspected
50 outbreaks of HeV along the Australian east coast, with documented annual outbreaks since 2006 [3].
51 Serological sampling of wild populations has identified pteropid fruit bats as the natural reservoir of
52 HeV [4,5]. While all recorded spillover events of HeV have occurred in Australia, the natural range of
53 pteropid bats extends much further north into Asia, potentially extending the at-risk area [6].
54 Indeed, sampling among bats and humans in Africa has uncovered neutralising antibodies in both
55 populations against HeV, as well as fellow genus members *Nipah henipavirus* (NiV) and *Ghanaian bat*
56 *henipavirus* (GhV) [7]. Seropositivity in humans was most common amongst individuals dealing in bat
57 bush meat or inhabiting areas of active deforestation [7], highlighting the increasing spillover risk of
58 emerging zoonotic viruses due to human encroachment on natural landscapes. HeV infection
59 typically exhibits a predominantly respiratory and neurological tropism, explaining the common
60 symptoms of HeV infection including pulmonary haemorrhage and oedema, encephalitis, and
61 meningitis and carries a mortality rate of 60-75% for both equine and human victims [8,9]. Disease
62 progression is generally rapid and most infected individuals die within days, or in the case of horses
63 are euthanised. However, one human case of recovery and subsequent fatal relapse 14 months after
64 infection has been reported that resembles the brain inflammation seen in persistent *Measles*
65 *morbillivirus* (MeV) infection [10]. Documented HeV transmission is predominantly through contact
66 with bodily fluids and the data reported on spillover events suggests that inter-equine transmission
67 can occur [1,2]. No direct transmission from bats to humans, or humans to humans, has yet been
68 described, with all human cases the result of contact with infected horses. However, highly
69 productive inter-human transmission of the closely related NiV has been observed in an outbreak
70 with a mortality rate of around 75%, suggesting that similar outbreaks of HeV with inter-human
71 transmission may occur in the future [11].

72 The HeV negative-sense single-stranded RNA genome is 18,234 nucleotides long, encodes six
73 genes, and conforms to the paramyxoviral 'rule of six' [12–14]. The first gene encodes the
74 nucleoprotein (N protein) which associates with the viral genomic and antigenomic RNAs to form the
75 helical nucleocapsid [14–16]. The nucleocapsid associates with the viral RNA dependent RNA
76 polymerase (RdRp) comprising the large (L) and phospho (P) proteins to form the holonucleocapsid.
77 The N-RNA interaction is critical for virus multiplication as genomic RNA is only recognised by the
78 RdRp as a template for mRNA transcription and genome replication when in the context of the
79 assembled nucleocapsid (reviewed in [17]), and incorporation of genomic RNA into new virions

depends on interactions between N protein within the nucleocapsid and the viral matrix (M) protein [17–19].

Paramyxoviral nucleocapsids, as well as those from the closely related family *Pneumoviridae*, classically exhibit a flexible, hollow, left-handed helical architecture under electron microscopy (EM), showing a characteristic herringbone pattern on transmission micrographs [20–26]. In these nucleocapsids, neighbouring N protomers laterally interact through their globular domains and completely encapsidate the viral genomic and antigenomic RNA within a continuous RNA binding cleft [27–29]. The N protomer of interest is topographically referred to as the index nucleoprotein (N_i) while the immediately adjacent protomers upstream and downstream of the N_i are referred to as index +1 N protein (N_{i+1}) or index -1 N protein (N_{i-1}), respectively. Each paramyxovirus N protomer covers exactly six RNA bases, which obeys the paramyxovirus 'rule of six', with the RNA bases generally following a 'three in, three out' binding register where three RNA bases are oriented in towards the RNA binding cleft and three RNA bases are oriented out towards the solvent [12,13,29–31]. Each helical turn of the paramyxoviral nucleocapsid comprises approximately 13 N protomers, although the exact number differs between viral species and is not necessarily an integer [21,26–29,31,32].

In addition to the extended helical nucleocapsid architecture, other atypical nucleocapsid assemblies have been observed in recent years. The formation of N protein-RNA ring complexes has been described for recombinantly-expressed nucleoproteins from various viruses, such as decameric N-RNA rings of *Human orthopneumovirus* (RSV) and *Vesiculovirus indiana* [25,33], undecameric N-RNA rings of *Lyssavirus rabies* [34], and tridecameric N-RNA rings of *Mammalian orthorubulavirus 5* [35]. Interestingly, features that resemble N-RNA rings were also observed packaged within RSV virions [36]. Furthermore, so-called 'clam-shell' nucleocapsid assemblies have been observed from recombinantly expressed nucleoproteins [32,37,38]. These clam-shells are formed by two helical nucleocapsids engaged in back-to-back stacking and have been found for *Avian orthoavulavirus 1* (formerly Newcastle disease virus; NDV), *Murine respirovirus*, and NiV [32,37,38].

Structural information on the HeV N protein and nucleocapsid assembly is scarce, collectively no more than a handful of negative-stain EM micrographs of isolated HeV nucleocapsids [39] or recombinantly expressed HeV nucleocapsid-like filaments [40] exist. While these confirm the similar herringbone morphology of HeV nucleocapsids to those of closely related viruses, a high-resolution reconstruction of the HeV N protein and nucleocapsid assembly has not yet been determined. Here, we report for the first time the HeV N protein structure in the context of a double-ring assembly as determined through cryoEM from recombinantly expressed HeV N protein.

113 The approach taken reveals the full HeV Ncore structure (residues 1-394) and further elucidates
114 established and novel paramyxoviral N-N and N-RNA interactions.
115
116

Results

Architecture of the HeV N protein-RNA assembly

HeV N protein was recombinantly expressed in *E. coli* and purified through IMAC using an N-terminally fused hexahistidine-SUMO affinity purification tag, followed by proteolytic removal of the affinity purification tag and subsequent SEC purification (Supplementary Figure S1). The purified HeV N sample was applied to cryo-grids and automated data collection was performed, including on-the-fly (OTF) pre-processing of the 3548 collected micrographs (Supplementary Figure S2) [41]. The micrographs contained a range of particles exhibiting circular and squat ring morphologies. Selection of these particles followed by 2D and 3D classification in RELION [42] revealed that these morphologies represent different orientations of the same multimeric N protein assembly, viewed across a 14-fold and 2-fold axis of symmetry, respectively (Supplementary Figure S3). Subsequent 3D refinement of a curated particle stack comprising 5638 particles and using D14 symmetry resulted in a 3.5 Å resolution EM density map, revealing a previously uncharacterised multimeric nucleoprotein assembly (Supplementary Figure S3, Supplementary Figure S4). The final map is a dimer of tetradecameric rings which enabled model building resulting in the first reported HeV N protein structure (Figure 1, Supplementary Figure S3, Supplementary Figure S4, Supplementary Table S1). In the HeV N protein assembly, two rings stack 'bottom-to-bottom', where the globular N-terminal domains (NTDs) intercalate to form a dimer of tetradecamers (Figure 1a-c). Each tetradecameric ring is topped with the C-terminal arms (Ct-arms) which cover parts of the globular C terminal domains (CTDs) (Figure 1a-c). The N-terminal arm (Nt-arm) lies completely within the particle's central cavity where it crosses over the NTD and interfaces with the back face of the CTD (Figure 1b).

Structure of the HeV N protein

The EM map of the HeV N protein assembly fully resolved the N protein core (Ncore), however no density was observed in the map corresponding to the intrinsically disordered C-terminal N protein tail (Ntail, Ala395-Val532). The HeV Ncore structure follows the common bi-lobed paramyxoviral N protein fold and includes the Nt-arm (Met1-Thr32), NTD (Thr33-Glu260), CTD (Glu261-His370), and Ct-arm (His371-Ala394), as well as bound *E. coli* host-derived RNA (Figure 1d-e). Both the Nt- and Ct-arm are linked to the globular domains by flexible loops and each forms an alpha helix in proximity to the CTD (Figure 1d). The N protein surface area is overall hydrophilic, with three prominent hydrophobic patches that are covered by neighbouring N protomers in the assembly (Supplementary Figure S5, Supplementary Figure S6). The Nt-arm alpha helix (α1) contains a strongly negatively charged, solvent-exposed region facing the central cavity consisting of residues Asp3, Asp6, and Glu7 (Figure 2).

151 **HeV N – N protein interactions in the multimeric assembly**

152 The HeV N protein double-ring assembly is formed through extensive lateral interactions in
153 each tetradecameric ring as well as intercalating interactions between two tetradecameric rings. The
154 lateral interfaces consist of electrostatic and hydrophobic interactions and are mediated primarily
155 through the Nt-arms, NTDs, and CTDs of two neighbouring N protomers, with contributions from the
156 Ct-arm, over a total buried surface area of ~2930 $Å^2$, calculated via PDBe PISA [43] (Supplementary
157 Figure S5, Supplementary Figure S6). At a calculated buried surface area of ~1195 $Å^2$, the N_i-N_{i+1}
158 interface mediated by globular domains represents just over a third of the total buried surface area
159 between the neighbouring protomers. The globular domain interface consists of extensive
160 electrostatic interactions, with the N_i surface containing mostly positively charged patches and the
161 N_{i+1} surface mostly negatively charged patches (Supplementary Figure S5). While the contribution of
162 the Ct-arm is minor, with a calculated buried surface area of only ~340 $Å^2$, the Nt-arm contributes
163 extensively to the lateral interactions. At a calculated buried surface area of ~1740 $Å^2$, this interface
164 represents just over half of the total lateral interface between N_i and N_{i+1}. Aside from electrostatic
165 patches, a conserved hydrophobic region consisting of a triad of aromatic residues (Phe267, Phe268,
166 and Tyr301) in the CTD of the N_i protomer and Phe11 in α1 of Nt-arm N_{i+1} protomer forms a key
167 interface [28,32] (Figure 3a). A further hydrophobic cleft in the N_i NTD (Tyr80, Ser81, Leu87, Val162,
168 Val165, Ile166, Ile234, and Val249) is occupied by the N_{i+1} Nt-arm loop Ala27-Thr33. Within this N_{i+1}
169 Nt-arm loop, residue Leu31 is buried inside a pocket in the N_i NTD consisting of Asn43, Arg48, Tyr80,
170 Glu82, Met158, Leu161, Val162, and Val165 (Figure 3b). Beyond the extensive N_{i+1} Nt-arm interface
171 with the Ni NTD and CTD, a minor contact exists between the utmost amino-terminal residues of the
172 N_{i+1} Nt-arm (Met1, Ser2, Ile4, and Phe5) and the N_{i-1} Ct-arm loop region Gln376-Lys381 (Figure 4).
173 This N_{+1}-N_{-1} interface represents a novel interaction that, to the best of our knowledge, has not been
174 described in the literature for paramyxoviral nucleocapsids and will be referred to as the 'elbow
175 interface'. Since the elbow interface only has a calculated buried surface area of ~80 $Å^2$, it is unlikely
176 to contribute strongly to N-N interactions. A defining feature of this HeV N protein double-ring
177 assembly is the gear-wheel interface between the two tetradecameric rings. This intercalation zone
178 consists solely of residues in the NTDs of N protomers in the top ring and N protomers in the bottom
179 ring (indicated by the lower-case n) (Figure 5). The N_i protomer contacts two protomers in the
180 bottom ring (n_i and n_{i+1}), with a total calculated buried surface area of ~545 $Å^2$. A clear, reciprocal
181 electrostatic interface exists between N_i and n_{i+1} with the residues Lys120, Glu123, and Glu124
182 where the two Glu residues in N_i form a tab that interacts with the Lys residue in n_{i+1} and *vice versa*
183 (Figure 5b). The poor electron density surrounding loop Met114-Asp119 forced the stubbing of side
184 chains and, accordingly, these were modelled as alanines (indicated in italics) (Figure 5b-c). An

185 electrostatic interaction may exist between the N_i Asp157 and n_i *Arg116*, as they are in proximity
186 and there is ample space for the Arg side chain. Similarly, N_i residues Ser44 and Glu46 form a patch
187 that may interact with n_i residues *Met114* and *Glu115* which are in close proximity. The absence of
188 clear electron density neither supports nor refutes these putative interactions and improved local
189 resolution may further elucidate the intercalation zone and increase the calculated buried surface
190 area.
191
192 **HeV N – RNA interactions**
193 The HeV N assembly map showed clear density for single-stranded RNA in the RNA-binding
194 cleft that separates the NTD and CTD, which was modelled as a poly-uridine; one hexa-uridine per N
195 protomer (Figure 6, Supplementary Figure S7). The RNA binding cleft contains hydrophobic patches
196 and is mostly positively charged near the RNA backbone and negatively charged near the RNA bases
197 (Supplementary Figure S5). The RNA molecule is oriented in the conventional 'three-base in, three-
198 base out' similar to other paramyxoviruses [28,29,32,35,37]. This orientation is facilitated by a 180°
199 turn of the RNA backbone every three nucleotides. In the case of HeV N, the 3'-most three-base
200 stack is oriented in towards the RNA-binding cleft while the 5'-most three-base stack are oriented
201 towards the solvent (Figure 6, Supplementary Figure S7. The charged RNA-binding cleft consists of a
202 cleft floor and two ridges that follow the orientation of the RNA chain (Figure 6a-c). Residue
203 segments Thr181-Gln200, containing α8, in the NTD and the loop Ser344-Tyr354 in the CTD form the
204 solvent-facing cleft ridges. The cleft floor consists of the NTD-CTD-connecting loop Glu260-Ala265
205 continuing into α12 until Arg272 as well as the α14-containing stretch Ser317-Gly326. Within the
206 RNA-binding cleft, a series of conserved basic (Lys178, Arg192, Arg193, Arg352) and polar (Thr185,
207 Gln199, Gln200, Tyr258, Gln319, Ser344, Tyr354) residues likely interact with the RNA chain through
208 electrostatic and hydrophobic interactions (Figure 6b-d) [28,29,32,35,37].
209 Adjacent to and contiguous with the RNA binding cleft floor is a large cavity surrounding the
210 inward facing three-base stack flanked by the N_i NTD and CTD as well as α13 of the N_{i+1} CTD and α1
211 of the N_{i+1} Nt-arm (Figure 7). While the modelled RNA bases are all uridines, this cavity – here called
212 the 'in-base cavity' – is sufficiently spacious to accommodate the larger purine bases and,
213 correspondingly, N_i residues Tyr258, Glu260, Glu261, Phe268, Ser344, and Met345, and N_{i+1} residue
214 Lys321 may be involved in interactions with these bases (Figure 7b).
215
216 **Comparison with other paramyxoviral N protein assemblies**
217 The HeV N protein fold resembles that of NiV N protein, its closest relative [8,14,32,44]. The
218 NiV N protein structure has been solved recently through cryoEM [32] and earlier through X-ray

219 crystallography [44]. Structural alignment of the HeV N protein model with the NiV N models reveals
220 some key differences (Figure 8). The global RMSDs for the HeV N protein structure compared to that
221 of the cryoEM-derived, RNA-bound NiV N protein structure and that of the NiV N protein structure
222 solved through X-ray crystallography are very similar (0.756 Å and 0.783 Å, respectively). In the NiV
223 X-ray structure, however, the NTDs and CTDs are rotated approximately 25° with respect to each
224 other compared to the HeV N and NiV cryoEM structures [32] resulting in a shift of the CTD of up to
225 15.5 Å at its greatest extent (Figure 8a). This rotation in the crystal structure is likely induced by
226 binding to the P protein Nt region which keeps the N monomers in an 'open' RNA-free conformation
227 (N^0) [16,44–47]. Three key differences appear from the alignment of HeV N with the two NiV N
228 structures. Firstly, the HeV N Nt- and Ct-arms in the double-ring assembly are shifted compared to
229 the Nt- and Ct-arms in the NiV N helical assembly (Figure 8b). Helical spiralling of a single split
230 tetradecameric ring would generate a nucleocapsid-like helix and inevitably requires some minor
231 conformational changes. The flexible nature of the Nt- and Ct-arm put them forward as suitable
232 candidates to provide those changes. Secondly, the solvent facing NTD alpha-helix 5 and its
233 succeeding loop (α5-loop) are also shifted compared to the homologous helix-loop in the NiV
234 structure (Figure 8b). In fact, this helix-loop region exhibits significant structural and sequence
235 variability among paramyxoviruses. Both its position and length are highly variable among the N
236 proteins of closely related paramyxoviruses, including *Mammalian orthorubulavirus 5* (formerly
237 human parainfluenza virus 5; PIV5), MeV, NDV, NiV, and SeV [29,32,35,37,38,44]. For example, the
238 HeV N protein α5-loop region contains two amino acid substitutions compared with the NiV N
239 protein; L108V and E137D, both of which are solvent exposed [32]. Whether there is a functional
240 relevance to these substitutions is unknown, however in the context of a helical nucleocapsid the
241 α5-loop region is the main solvent exposed section of the N protomer and may be important for
242 interactions with the RdRp complex during transcription and replication, or could potentially
243 interface in-phase with the M protein lattice during virion assembly, as proposed for other
244 paramyxoviruses [17–19]. Furthermore, the α5-loop region has also been identified as the main
245 interface in intercalating interactions in the HeV N protein assembly (Figure 5), as well as in clam-
246 shell formation in NDV, NiV, and SeV nucleocapsid-like filaments (NLFs) [32,37,38]. The intercalating
247 interface observed in the HeV N double-ring assembly suffered from local poorly resolved electron
248 density (Supplementary Figure S4), which abrogated confident model building and forced the
249 stubbing of residue side chains for *Met114*, *Glu115*, *Arg116*, *Arg117*, and *Asp119*. This poor local
250 density may reflect the existence of weak interactions within the interface since stronger
251 interactions would rigidify the loop side chains and by extension produce clearer density. The
252 modelled alanines likely do not accurately portray the potential for extensive interactions these

253 residues may engage in with neighbouring N protomers. Indeed, residues homologous to these have
254 been identified as putative drivers of clam-shell interactions in the paramyxoviruses NDV, NiV, and
255 SeV [32,37,38]. Focussed refinement on this area failed to improve map resolution, and likely
256 reflects – in part – the inherent flexibility of both this loop and the intercalating interface. Similarly,
257 local resolution around the HeV N protein Ct-arm α17 was poor and while an alpha helix could
258 confidently be built into the density, a number of side chains were also stubbed and modelled as
259 alanines. Finally, more Ct-arm residues are resolved in the helical NiV N protein structure than in the
260 HeV N double-ring structure, while the HeV N protein structure shows the very N-terminal Met1
261 residue where the NiV N protein structure cuts off at Ile4 [32]. Comparison of the cognate region in
262 protein structures from related viruses revealed that the extreme N-terminal residues are either
263 distended away towards the central cavity as in NDV [37] or are completely absent as for PIV5, NiV,
264 MeV, and SeV [29,32,35,38] (Figure 8c-f). The shift in orientation or complete absence of the
265 extreme N-terminal residues may be due to the presence of remaining N-terminal affinity tags that
266 limit local cryoEM resolution. Indeed, an N-terminal affinity purification tag remained attached to
267 resolved N protein structures for PIV5, NDV, NiV, and SeV [32,35,37,38] while the MeV purification
268 used a C-terminal tag [29]. The tag-free N-terminal residues in the HeV double-ring assembly were
269 identified as a potential minor interface (Figure 4). This elbow interface likely exists in NiV N protein
270 assemblies as well, and the data suggest a similar interface may occur in more distantly related
271 viruses such as PIV5 and MeV [29,35].
272
273 **Discussion**
274 The emergence of novel pathogens such as HeV is accompanied by gaps in fundamental
275 knowledge and technical resources. It is therefore of paramount importance to increase these key
276 assets prior to an outbreak. While preparedness systems are falling into place for HeV, including
277 surveillance, diagnostic tools and laboratory confirmation, and treatment and prevention, many
278 questions regarding the molecular biology of HeV remain unanswered.
279 Following cryoEM data collection, a multimeric HeV N protein double-ring assembly was
280 resolved to 3.5 Å resolution, enabling the building and refinement of an atomic HeV N protein
281 model. Paramyxoviral double-ring complexes may represent a convergent architecture that reflects
282 the need for 5' capping of genomic and antigenomic nucleocapsids, the need to encapsidate leader
283 sequences, and the need for short-term metastable N protein storage. The elucidation of the HeV N
284 protein structure allowed for the identification of differences between it and related viral N protein
285 structures, but importantly may also highlight commonalities that can be exploited for the design of
286 new, broad-acting therapeutics.

287 The paramyxoviral nucleocapsid assembly entirely covers the viral genome, protecting it
288 from detection and degradation by host factors and serving as the template for viral mRNA
289 transcription and genome replication. Here, we determined the cryoEM structure of the
290 recombinantly expressed, full-length and tag-free HeV N protein in complex with *E. coli* host-derived
291 RNA. This structure is, to our best knowledge, the first high-resolution structure of the HeV N protein
292 at 3.5 Å resolution and the first formal description of a paramyxoviral N protein double-ring
293 assembly.

294 Overall, the HeV N protein fold resembles closely and more distantly related paramyxoviral
295 N protein structures, including the recently solved N protein structures of PIV5 [35], MeV [29], NDV
296 [37], and SeV [38], with its closest structural and genetic match being NiV N [32,44]. The N protein
297 consists of an Ncore region and an intrinsically disordered Ntail, and, as is common for
298 paramyxoviral N proteins, only the Ncore region was well resolved with no clear cryoEM density
299 representing the Ntail. The HeV N protein shares around 92% amino acid identity with the NiV N
300 protein [8,14,32,44]. The crystal structure for NiV N was solved as a truncated protein – missing both
301 the Nt- and Ct-arms – and in complex with the Nt region of the NiV P protein [44]. More recently, the
302 full NiV Ncore structure was solved through cryoEM from helical particles [32].

303 Structural alignment of the final HeV N protein model (PDB: 8CBW) with both the NiV N
304 protein crystal structure (PDB: 4CO6) and cryoEM structure (PDB: 7NT5) revealed a globally similar
305 protein fold, with some key differences. The most prominent of these differences is the
306 approximately 25° rotation and up to 15.5 Å shift in the CTD, which is the result from the open, apo-
307 configuration of the P protein-bound NiV N (P-N^0) complex in the NiV N crystal structure [44]. Since
308 the cryoEM NiV N structure is RNA-bound [32], it offers a better comparison with the similarly RNA-
309 bound HeV N structure. A slight shift in the orientations of both the Nt- and Ct-arms likely stems
310 from the differences in overall multimeric morphology, since the NiV structure originates from a
311 helical segment with ~13.2 N protomers per helical turn, while the HeV structure is drawn from a 14
312 N protomer-containing flat ring within the double-ring particle. Helical spiralling of a single, split
313 tetradecameric ring would generate a helix resembling that of NiV and inevitably incur some minor
314 conformational changes likely engendered by the flexible Nt- and Ct-arms whilst maintain a
315 relatively static globular domain fold.

316 Furthermore, the NiV N Ct-arm has resolved four additional residues compared to the HeV N
317 protein structure, while the HeV N protein structure resolves the extreme N-terminal Met residue
318 where the NiV N protein structure terminates at Ile4 [32]. Similarly, the extreme N-terminal residues
319 are often absent in N protein structures from other, related viruses, including PIV5, MeV, and SeV
320 [29,35,38]. The resolution of the extreme N-terminal residues in the HeV N structure enabled the

321 identification of a novel, albeit likely weak, interaction surface between the N_{i+1} and N_{i-1} protomers
322 here called the elbow interface. The presence of an elbow interface in the N protein assemblies of
323 PIV5, MeV, NiV, and SeV is likely obscured due to the absence of the extreme N-terminal residues in
324 these structures. Where the expression and purification pipeline for HeV N included an affinity-tag
325 removal step to generate a native protein sequence, those for the viral N proteins listed above did
326 not. As a result, the presence of remaining, unstructured, N-terminal affinity tags may locally limit
327 cryoEM resolution and fail to depict the elbow interface. This hypothesis is further supported by the
328 N protein structure of NDV which does resolve the extreme N-terminal residues, but these face away
329 from the putative elbow interface and towards the central cavity [37], likely due to the presence of
330 an N-terminal affinity tag.

331 Finally, the solvent facing HeV NTD alpha-helix 5 (α5) and its succeeding loop show
332 significant structural and sequence variability among paramyxoviruses and its position and length
333 are highly variable among the N proteins of closely related paramyxoviruses, including MeV, NDV,
334 NiV, PIV5, and SeV [29,32,35,37,38,44]. Compared to the cryoEM NiV N structure, the HeV α5-loop
335 region contains two amino acid substitutions compared with the NiV N protein; L108V and E137D,
336 both of which are solvent exposed [32]. In the context of a helical nucleocapsid, this solvent-exposed
337 helix-loop region is likely important for interactions with both the RdRp complex and the M protein
338 at various stages of the viral life cycle [17,48]. Furthermore, the α5-loop region is also part of the
339 intercalating interface in the HeV double-ring assembly and in the clam-shell assemblies found for
340 NDV, NiV, and SeV [32,37,38].

341 While the experimental particle stack only contained 5683 particles, D14 symmetry
342 imposition resulted in an effective 157,864 asymmetric units. Symmetrised reconstructions often
343 struggle to resolve regions of structural or compositional heterogeneity, and their signal may be
344 diluted compared to the less heterogenic regions. In the reconstruction of the HeV N protein
345 assembly, some of these heterogenic regions, foremost Met114-Asp119, are poorly resolved and as
346 a result hindered confident model building of side chain residues. The electron density in the RNA
347 binding cleft, identified through comparison with homologous structures, enabled *de novo* modelling
348 of a hexameric RNA chain in the asymmetric unit. The electron density unambiguously identified the
349 RNA backbone and the general location of the bases, but not their identities. This is to be expected
350 due to both the presence of random host-derived RNA and symmetrised averaging of that RNA.
351 Individual HeV N protein double-ring assemblies are unlikely to have complete occupancy by
352 bacterial host-derived RNA over each of the 28 N protomers. Any RNA-free N protomers in the
353 assembly would be outnumbered by RNA-bound protomers and as a result are averaged out against
354 them, evidenced by the clear RNA density. Non-symmetrised particles would likely shed more light

355 on both the uniformity of RNA occupancy as well as regions of structural flexibility with the
356 requirement for larger particle stacks.

357 The RNA occupying the RNA binding cleft was modelled as one hexa-uridine per N protomer,
358 adhering to the convention for paramyxoviral N proteins. The typical 3' to 5' 'three in, three out'
359 base stacking orientation observed in other paramyxoviral N proteins is also found in the HeV N
360 assembly, where bases 1, 2, and 3 face in towards the protein and bases 4, 5, and 6 are solvent
361 exposed. Furthermore, a series of basic (Lys178, Arg192, Arg193, Arg352) and polar (Thr185, Gln199,
362 Gln200, Tyr258, Gln319, Ser344, Tyr354) residues were identified as putatively interacting with the
363 RNA chain through electrostatic and hydrophobic interactions. While most of these interactions are
364 with the RNA backbone, a key, conserved interaction occurs between RNA bases 5 and 6 and the
365 amino acid dyad Gln199 and Gln200 which HeV N shares with the N proteins from MeV, NiV, and
366 PIV5 [29,32,35]. Additionally, a conserved in-base cavity is contiguous with the RNA binding cleft,
367 consisting of two neighbouring N protomers and can accommodate larger purines in the in-base
368 stack comprising nucleotides 1, 2, and 3. Putative interactions with residues Tyr258, Glu260, Glu261,
369 Phe268, Lys 321, Ser344, and Met345 may facilitate purine binding where pyrimidines are too
370 distant. A homologous cavity exists in closely related N protein assemblies, such as NiV, NDV, and
371 MeV [29,32,37] and merits further investigation as a potential therapeutic target.

372 While N-RNA interactions are thought to be sequence non-specific and HeV N model
373 building was done in a sequence-agnostic manner, some evidence for MeV suggests RNA
374 encapsidation exhibits a preference for purine-rich sequences and importantly, the antigenomic
375 leader sequence [49]. Similar preferences for purine rich and leader-specific RNA were also observed
376 for the more distantly related RSV and VSV, respectively [50,51]. Indeed, the HeV genomic and
377 antigenomic leader sequences are purine rich as well, with ~70% and ~63% purines for the genomic
378 and antigenomic leaders, respectively. Moreover, the terminal six nucleotides of the HeV genomic
379 and antigenomic leaders are identical (5'-ACCGAA) [14]. Additional interactions with these purine
380 bases both in the in-base cavity as well as in the region of bases 5 and 6 may drive this difference in
381 specificity and be important factors in the initial stages of 5' encapsidation of the nascent genome as
382 it emerges from the RdRp complex. As a result, the in-base cavity and the RNA binding cleft may
383 present a target for the development of therapeutics that abrogate the critical step of RNA-
384 encapsidation in the paramyxoviral life cycle.

385 HeV, discovered in 1994, is the type species for the genus *henipavirus* in the family
386 *Paramyxoviridae* [52]. Emergent zoonotic outbreaks and surveillance of wild populations have
387 expanded the genus with NiV, *Cedar henipavirus* (CedV), *Mojiang heninpavirus* (MojV), and
388 *Ghanaian bat henipavirus* (GhV) [53–55] and over the past few years with the discovery of four new

species; *Gamak henipavirus* (GAKV), *Daeryong henipavirus* (DARV), *Langya henipavirus* (LaV), and *Angavokely henipavirus* (AngV) [56–58]. The recent discovery of a novel HeV strain in Australia, called HeV-var [59], as well as the addition of four new henipaviral species in the past 3 years, highlights the needs for continued surveillance and research into this genus and HeV specifically. With around 88% sequence identity for the HeV-var N gene sequence compared to the HeV reference strain (NCBI RefSeq: NC_001906), a total of 18 amino acid substitutions were found of which 13 lie in the intrinsically disordered Ntail region (Supplementary Figure S8). Five substitutions are located in the Ncore region; S2G, D6E, and S13N in the Nt-arm, L153M in the NTD, and S386P in the Ct-arm (Supplementary Figure S8). Both D6E and S13N face the solvent of the double-ring central hole, however Ser2 forms part of the putative elbow interface between the N_{i-1} and N_{i+1} neighbours (Figure 4). The S2G substitution in HeV-var could abrogate this elbow interface. The NTD-located L153M substitution sits at the upper surface of the NTD facing the exterior solvent and is unlikely to be involved in intercalation zone interactions. Finally, the S386P substitution in the Ct-arm faces the solvent in the double-ring assembly, but likely forms part of the interface between successive helical turns in the nucleocapsid assembly. These interactions are thought to contribute minimally to nucleocapsid stability due to the nucleocapsid's inherent flexibility and the observation that each helical turn consists of a non-integral number of N protomers [27]. Interestingly, no substitutions were described in the α5-loop region, which normally exhibits significant structural and sequence variability among paramyxoviruses. Taken together, the amino acid substitutions in the Ncore observed in the HeV variant strain likely have a minimal impact on HeV nucleocapsid formation and architecture. The large number of substitutions in the intrinsically disordered Ntail region, especially towards the C-terminus, could indicate a changed interaction with the RdRp complex and M proteins however these assumptions still await experimental validation.

The dimer of tetrameric rings that form the HeV N protein double-ring assembly is, to our best knowledge, a unique paramyxoviral N protein architecture that lacks a formal description in the current literature. However, other paramyxoviral N protein architectures have been observed that are reminiscent of the double-ring assembly. N protein clamshell interfaces have been described, in detail, for the paramyxoviruses NDV, NiV, and SeV NLFs [32,37,38]. In these cases, recombinant expression of N proteins revealed clamshell interfaces as both discrete particles reminiscent of, but distinct from, the double-ring assemblies [32,37] as well as part of a so-called double-headed helix; two anti-parallel NLFs stacked bottom-to-bottom and following the NLF's helical register [37,38]. While a similar loop region is involved in these interactions in all three, the specifics of the clamshell architectures differ between the three reports. In the case of NDV, the N protomers that constitute the clamshell are positioned vertically in line and do not intercalate [37]. Those described for SeV

423 appear to have two forms, called 'closed' and 'hyper-closed', where the level of intercalation is
424 higher for the hyper-closed state [38]. Finally, the NiV clamshell exhibits extensive intercalation
425 similar to the HeV double-ring assembly [32]. Furthermore, while in each of these cases the two
426 faces of the clamshell follow the helical register of the NLF, an additional small population of NiV
427 clamshells have been observed where the ~13.2 N protomer helix is capped with a flat
428 tetradecameric ring [32]. This ring closely matches one half of the HeV double-ring assembly.
429 Importantly, the presence of double-headed helices was confirmed from virus-extracted
430 nucleocapsids of SeV [38] and the inability to form double-headed nucleocapsids was detrimental to
431 EGFP reporter gene expression in an NDV minigenome-based replicon assay [37].

432 The double decameric N protein rings of RSV, a member of the family *Pneumoviridae*, has
433 recently been resolved through cryoEM [60]. In this RSV N protein assembly, akin to HeV, two N
434 protein rings stack in a bottom-to-bottom orientation. Interestingly, the two rings do not intercalate
435 to an appreciable degree and instead interact solely through the tips of the NTDs. The RSV N_i thus
436 only interacts with one N protomer in the opposite ring (n_i) where in the HeV N double-ring
437 assembly the N_i protomer interacts with two N protomers (n_i and n_{i+1}). As a consequence, the RSV
438 double-ring assembly exhibits ten apertures along the interface between the two rings that made up
439 of the NTDs of N_i, N_{i-1}, n_i, and n_{i+1} which are over 13 Å wide at their narrowest point Interestingly, a
440 recent paper describes the presence of single-faced closed-ring N protein assemblies inside RSV
441 virions [36]. Although of lower resolution due to the use of cryo-ET, these rings bear a striking
442 resemblance to the single and double decameric rings observed for recombinantly expressed RSV N
443 protein [25,26,60] and indeed one tetradecameric half of the HeV double-ring assembly. Their
444 abundance in RSV virions hints at a potential physiological relevance. While the occupancy and
445 identity of RNA in these virion-enclosed rings was not confirmed, it is known that in RSV-infected
446 cells short, 21 to 25 nucleotide-long RNAs generated from the genomic leader and trailer sequences
447 are among the most abundant viral RNAs present [61–63]. Furthermore, some of these RNAs are
448 resistant to nuclease treatment, indicating they may be encapsidated [62].

449 The occurrence of N protein double-rings and the related clamshells in recombinantly
450 expressed N protein samples could be an artefactual result of the method of sample generation.
451 However, the presence of clamshells in virion-extracted nucleocapsids [38] and of N protein ring
452 assemblies inside virions [36] suggests otherwise. A picture emerges where the double-ring
453 assembly may be indicative of one or multiple of a number of viral processes.

454 Firstly, it is hypothesised that the occurrence of clamshell interfaces both protects the viral
455 genome from nuclease and protease attack and drives the inclusion of multiple copies of the viral
456 genome into nascent virions [17,37,38]. Interestingly, these clamshells appear to join only the 5'

457 ends, which are the first to emerge from the RdRp during genome replication and may be the most
458 vulnerable to degradation. Furthermore, polyploidy is increasingly recognised in a wide range of
459 members of the order *Mononegavirales* [64–67] and clamshell interfaces may explain this
460 occurrence at least partially. The double-ring resembles these clamshells, in particular the flat ring of
461 the semi-spiral clamshell interface found in NiV N assemblies, and the double-ring assembly may
462 therefore be a by-product of the viral need for genomic 5' nucleocapsid capping.

463 Secondly, the high abundance of complementary leader and trailer RNAs in virus-infected
464 cells could result in the activation of the innate immune response. The encapsidation of these
465 sequences is hinted at for RSV [62], which could shield them from detection by the innate immune
466 system. Interestingly, the 56 nt-long HeV leader sequence, which is transcribed and separated from
467 the mRNA transcripts during the RdRp transcription mode, falls within the occupancy range for a
468 single tetradecameric ring (84 nt). This purine-rich sequence is also likely preferentially encapsidated
469 over RNA chains with an even purine-pyrimidine ratio [49–51]. The HeV trailer sequence is shorter
470 than the leader and similarly rich in purine bases. An antagonistic function in stress granule
471 formation and cellular apoptosis and has been reported for the (released) trailer sequence in SeV
472 and RSV [68,69] and a similar function could exist for the HeV trailer. Whether putative
473 encapsidation of the trailer aids or hinders this function is unclear, but encapsidation of both the
474 leader and the trailer could permit inclusion into progeny virions and subsequent release in newly
475 infected cells to perform their suggested antagonistic functions without immediate the requirement
476 for viral RNA transcription.

477 Thirdly, single or double N-RNA rings such as the HeV double-ring assembly, could play a role
478 in nucleating liquid-liquid phase separation for biomolecular condensates and aid in the formation of
479 viral transcription/replication centres [70,71]. Evidence has been found for this process in RSV and
480 has recently been investigated in detail for MuV where a combination of cryo-ET, fluorescence
481 microscopy, and mass spectrometry reveal a stress-induced modulation of phase-separated N-P
482 complexes [72]. A similar role may exist for the HeV double-ring assembly during phase separation in
483 HeV infected cells.

484 Finally, the HeV N protein double-ring, and indeed N protein rings observed elsewhere, may
485 reflect the need for short-term, reversible storage of N protomers in the absence of abundant P
486 protein chaperones. Indeed, the P protein engages in extensive interactions with N protomers to
487 maintain them in an open, apo-state (N^0). Re-initiation of transcription by the RdRp complex is
488 inefficient and as a result viral mRNA abundance is inversely correlated to the distance from the
489 genomic 3'-end [17,73,74]. Consequently, the abundance of non-nucleocapsid-bound N protein is
490 likely much higher than that of P protein and there is the potential for excessive N protein

491 concentrations inside the infected cell. The formation of double-ring assemblies, either RNA-bound
492 or in the apo-state, could therefore provide a short-term, metastable, multimeric N protein storage
493 where P protein shuttles between them and the RdRp complex during active encapsidation of
494 nascent genomic or antigenomic RNA.
495
496 **Materials and Methods**
497 **Cloning *Hendra henipavirus* N gene into bacterial expression vectors**
498 The HeV N gene sequence was taken from the reference *Hendra henipavirus*
499 genome (NCBI Reference Sequence: NC_001906.3), codon-optimised for recombinant expression in
500 *Escherichia coli* hosts, flanked by 5' *Bam*HI and 3' *Xho*I restriction sites, and supplied in pTwist (Twist
501 Bioscience). Following digestion with *Bam*HI and *Xho*I, the restriction fragment was subcloned into
502 pET-28a-6His-SUMO so that the HeV N protein coding region is downstream of the hexahistidine
503 (6xHis) affinity tag and SUMO protease recognition sequence, with the resulting plasmid confirmed
504 as correct by Sanger sequencing (Genewiz). The *Escherichia coli* (*E. coli*) DH5-α strain (Thermo Fisher
505 Scientific) was used for plasmid amplification. Sequencing and amplification primers were designed
506 using Benchling and ordered through Integrated DNA Technologies. Plasmid DNA was purified using
507 a QIAprep Spin Miniprep kit (Qiagen) or QIAGEN Plasmid Midi kit (Qiagen) according to the
508 manufacturer's instructions. Where appropriate, products were resolved by agarose gel
509 electrophoresis, excised from the gel and purified using a QIAquick Gel Extraction kit (Qiagen)
510 according to the manufacturer's instructions.
511
512 **Recombinant protein expression**
513 *E. coli* BL21-Rosetta 2(DE3)pLysS (Novagen) transformed with pET-28a-6His-SUMO-HeVN
514 was inoculated in a 1/500 ratio into 2xYT medium with kanamycin (16 gr/l Tryptone Plus (Sigma
515 Aldrich), 10 gr/l Yeast Extract (Sigma Aldrich), 10 gr/l NaCl (Fisher Scientific), 50 µg/ml Kanamycin
516 (Bio Basic)) and grown at 37°C in a Multitron Standard incubator (Infors HT) until reaching an OD_{600}
517 of 0.5, at which point the growth temperature was reduced to 26°C and the inoculi were further
518 grown until an OD_{600} of 0.8 was reached. Expression of HeV N was then induced by addition of 0.5
519 mM IPTG (ChemCruz) and cultures were further incubated for 4 hours at 26°C. Cultures were
520 harvested by centrifugation for 25 minutes at 4500 rpm in an Avanti J26-XP with JLA 8.1000 rotor
521 (Beckman Coulter).
522 Harvested pellets were resuspended in 30 ml lysis buffer (20 mM Tris-HCl pH 7.5
523 (ChemCruz), 500 mM NaCl, 20 mM Imidazole (Acros Organics), 0.1% v/v Triton X-100 (SAFC)) and
524 subjected to one freeze-thaw cycle (-80°C to +40°C). The lysis buffer was then supplemented with

525 cOmplete Mini Protease Inhibitor cocktail tablets (Sigma Aldrich), 10 µg/ml DNase I (Roche), 20
526 µg/ml RNase A (Invitrogen), and 0.25 µg/ml Lysozyme (Sigma Aldrich) and incubated for 30 minutes
527 on ice with a magnetic stirrer. Lysates were sonicated for 10 cycles of 15 seconds on, 45 seconds off
528 using the SoniPrep 150 Ultrasonic Disintegrator with External Process Timer (MSE), then transferred
529 to ultracentrifuge tubes and centrifuged for 45 minutes at 16000 rpm and 4°C in an Evolution RC
530 with SA300 rotor (Sorvall). The soluble fraction was collected in 50 ml falcon tubes and carried
531 forward to purification.
532
533 **Affinity chromatography**
534 Soluble fractions were passed through a primary HisTrap HP 5 ml column (GE Healthcare),
535 previously equilibrated with column buffer (20 mM Tris-HCl pH 7.5, 500 mM NaCl, 20 mM
536 Imidazole), using a 101U/R peristaltic pump (Watson Marlow). The column was washed with
537 multiple washes of 25 ml column buffer with increasing concentrations of imidazole (20 mM, 50
538 mM, 100 mM, 300 mM, and 500 mM). The flow-through of the soluble fraction and each of the wash
539 fractions was collected in full. The presence of protein was confirmed with Bradford Assay (Bio-Rad),
540 NanoDrop One (Thermo Fischer Scientific), and SDS-PAGE analysis.
541 Fractions containing the majority of the Hev N protein were transferred into Spectra/Por 3
542 Standard RC Tubing (MWCO 3.5 kDa) (Spectrum). In-house recombinantly-expressed hexahistidine-
543 tagged SUMO protease (Ulp1) was added to the dialysis tubing and fractions were dialysed overnight
544 against dialysis buffer (20 mM Tris-HCl pH 7.5, 300 mM NaCl) at 4°C. SUMO protease cleavage was
545 confirmed via SDS-PAGE analysis and the dialysed, cleaved mix was sterile filtered using a Minisart
546 NML Syringe filter 0.45 µm SFCA (Sartorius) and passed through a secondary HisTrap column. The
547 flow-through was collected and kept on ice, and the column was washed with pre-chilled low- and
548 high-imidazole washes. The flow-through was sterile filtered and concentrated to a final volume of 7
549 ml using Amicon Ultra-15 Centrifugal filter concentrator (Merck Millipore).
550
551 **Size exclusion chromatography**
552 Size exclusion chromatography (SEC) was performed using an ÄKTAprime Plus with HiPrep
553 26/60 Sephacryl 400 HR column (GE Healthcare) at 4°C, previously equilibrated with degassed and
554 filtered SEC buffer (25 mM Tris-HCl pH 7.5, 100 mM NaCl). Fractions of 2.5 ml were collected
555 following an 80 ml void volume. Presence of HeV N protein was confirmed with SDS-PAGE analysis.
556 Concentrations and 260/280 ratios were determined and fractions containing HeV N protein were
557 either directly used for electron microscopy (see below) or flash frozen and stored at -80°C.
558

559 **Preparation of cryo-grids**

560 Copper Ultrathin Carbon (UC) Lacey grids (Agar Scientific) were glow discharged for 30
561 seconds at 10 mA on an easiGlow Glow Discharge Cleaning System. 3 µl protein sample at 1 mg/ml
562 concentration was applied to the grids and plunge frozen into liquid ethane cooled in liquid nitrogen
563 using an FEI Vitrobot Mark IV (Thermo Fisher Scientific; blot force 6, blot time 6-8s, humidity 95-
564 100%).

565

566 **Data collection on cryo-grids**

567 Data was collected on an FEI Titan Krios (X-FEG) TEM (Thermo Fisher Scientific) (ABSL,
568 University of Leeds) operated at 300 keV with a Falcon III direct electron detector in integrating
569 mode (Thermo Fisher Scientific), at a nominal magnification of 75000x and a pixel size of 1.065 Å.
570 Further data acquisition parameters are shown in Supplementary Figure S2. 3548 micrographs were
571 taken at a total dose of 59.7 e/Å^2 split into 55 fractions and a defocus range of -0.7 to -2.8 µm. A
572 detailed description of the data collection pipeline has been published [41]. Micrographs were
573 visualised in ImageJ or RELION 3.1.1.

574

575 **Electron microscopy data processing and single particle analysis**

576 The dataset of 3548 micrographs was collected using an automated approach and pre-
577 processed on the fly during collection using the RELION software suite [41,42]. Motion correction
578 and CTF estimation were carried out using RELION-integrated implementations of MotionCor2
579 (v1.2.1) [75] and Gctf (v1.18) [76], respectively. Following pre-processing, particles coordinates were
580 manually selected using the manual picking job following the single-particle analysis (SPA)
581 procedure. 3D maps were visualised in UCSF Chimera [77] and UCSF ChimeraX [78,79].

582 Using single particle analysis, a total of 3500 particles were selected from a random subset
583 of 502 micrographs to generate a reference for automated picking through 2D classification.
584 Reference-based automated picking was then optimised for picking threshold, maximum stddv
585 noise, and minimum avg noise values, resulting in 875,262 selected particles, extracted using a box
586 size of 360 pixels (383.4 Å). Multiple rounds of 2D classification were carried out to enrich the
587 particle stack with true particles and removing junk particles. The high-resolution 2D classes
588 revealed the presence of both a C2 and a C14 symmetry axis, for a combined D14 symmetry in the
589 double-ring particle.

590 An initial 3D reference map was generated *de novo* by stochastic gradient descent (SGD) and
591 used for 3D classification and 3D refinement. Manual re-alignment and resampling of the C1
592 symmetry refined 3D map to the grid of the unaligned map in UCSF Chimera [77] enabled D14

593 symmetry imposition in subsequent 3D jobs. The C1 symmetry refined 3D map was then used as a
594 3D reference map for subsequent D14 symmetry-imposed 3D classification and refinement jobs. A
595 solvent mask was generated from the 3D class in Relion, using a lowpass filter of 15Å, an initial
596 binarisation threshold of 0.012, a 3 pixel binary map extension, and a 3 pixel soft-edge. In post-
597 processing, this solvent mask was applied to the refined cryoEM map to counter the influence of
598 high-resolution noise to improve map quality and improve estimated resolution. The final EM map
599 was deposited in the EMDB under accession EMD-16426.
600
601 **Atomic protein model refinement and interpretation**
602 The cryoEM density map was of sufficient quality to allow the building and refinement of an
603 atomic model. SWISS-MODEL [80] was used to predict an initial model based on homology search
604 with PDB: 4CO6 [44], the closest match at the time of processing. The homology model was input for
605 automated model building in Buccaneer [81]. The Buccaneer model was imported into Coot v0.9.4
606 [82,83] for manual refinement. High-resolution density enabled *de novo* building of a hexameric RNA
607 chain modelled as poly-uridine following nucleoprotein structure convention. Multiple rounds of
608 automated real-space refinement in Phenix v1.20.1 [84,85] and manual adjustment in Coot resulted
609 in the final model. Manual adjustments were carried out on a single monomer in Coot which was
610 then symmetry expanded in UCSF Chimera v1.15 according to D14 symmetry prior to real-space
611 refinement to prevent erroneous refinement into non-cognate density. Poor local density abrogated
612 confident side chain placement and forced the stubbing of some amino acids, which were modelled
613 as alanines in the final model. Model validation was carried out as part of the final real-space
614 refinement job through MolProbity [86,87] integrated within Phenix. Atomic models were deposited
615 with the Protein Data Bank under accession 8C4H for the complete double-ring assembly and 8CBW
616 for the asymmetric protomer unit.
617 Interaction surfaces were calculated through PDBe PISA v1.52 [43] and 3D atomic models
618 were visualised in UCSF ChimeraX v1.2.5 [78,79].
619

620 **Data Availability Statement**

621 The refined cryoEM map was deposited with the EMDB under accession EMD-16426. Atomic models
622 were deposited with the Protein Data Bank under accession 8C4H for the complete double-ring
623 assembly and 8CBW for the asymmetric protomer unit.

624

625 **References**

626

627 [1] Murray, K. et al. A morbillivirus that caused fatal disease in horses and humans. Science (80-.
628). **268** 94–97 (1995). https://doi.org/10.1126/science.7701348.

629 [2] Selvey, L.A. et al. Infection of humans and horses by a newly described morbillivirus. Med. J.
630 Aust. **162** 642–645 (1995). https://doi.org/10.5694/j.1326-5377.1995.tb126050.x.

631 [3] Queensland Government Summary of Hendra virus incidents in horses. Bus. Queensl.
632 Website. (2022). https://www.business.qld.gov.au/industries/service-industries-
633 professionals/service-industries/veterinary-surgeons/guidelines-hendra/incident-summary
634 (accessed July 14, 2022).

635 [4] Young, P.L. et al. Serologic Evidence for the presence in Pteropus Bats of a Paramyxovirus
636 Related to Equine Morbillivirus. Emerg. Infect. Dis. **2** 239–240 (1996).
637 https://doi.org/10.3201/eid0203.960315.

638 [5] Halpin, K., Young, P.L., Field, H.E., Mackenzie, J.S. Isolation of Hendra virus from pteropid
639 bats: A natural reservoir of Hendra virus. J. Gen. Virol. **81** 1927–1932 (2000).
640 https://doi.org/10.1099/0022-1317-81-8-1927.

641 [6] World Health Organization Geographic distribution of Marburgh haemorrhaigc fever
642 outbreaks and fruit bats of Pteropodidae Family. (2008).
643 https://www.who.int/images/default-source/health-topics/marburg-virus-disease/marburg-
644 virus-disease-map-2009.png?sfvrsn=2718bf75_0.

645 [7] Pernet, O. et al. Evidence for henipavirus spillover into human populations in Africa. Nat.
646 Commun. **5** 5342 (2014). https://doi.org/10.1038/ncomms6342.

647 [8] Eaton, B.T., Broder, C.C., Middleton, D., Wang, L.F. Hendra and Nipah viruses: Different and
648 dangerous. Nat. Rev. Microbiol. **4** 23–35 (2006). https://doi.org/10.1038/nrmicro1323.

649 [9] Playford, E.G. et al. Human Hendra virus encephalitis associated with equine outbreak,
650 Australia, 2008. Emerg. Infect. Dis. **16** 219–223 (2010).
651 https://doi.org/10.3201/eid1602.090552.

652 [10] O'Sullivan, J.D. et al. Fatal encephalitis due to novel paramyxovirus transmitted from horses.
653 Lancet. **349** 93–95 (1997). https://doi.org/10.1016/S0140-6736(96)06162-4.

654 [11] Gurley, E.S. et al. Person-to-person transmission of Nipah virus in a Bangladeshi community.
655 Emerg. Infect. Dis. **13** 1031–1037 (2007). https://doi.org/10.3201/eid1307.061128.
656 [12] Calain, P., Roux, L. The rule of six, a basic feature for efficient replication of Sendai virus
657 defective interfering RNA. J. Virol. **67** 4822–4830 (1993).
658 https://doi.org/10.1128/jvi.67.8.4822-4830.1993.
659 [13] Kolakofsky, D. et al. Paramyxovirus RNA Synthesis and the Requirement for Hexamer Genome
660 Length: the Rule of Six Revisited. J. Virol. **72** 891–899 (1998).
661 https://doi.org/10.1128/jvi.72.2.891-899.1998.
662 [14] Wang, L.-F. et al. The Exceptionally Large Genome of Hendra Virus: Support for Creation of a
663 New Genus within the Family Paramyxoviridae . J. Virol. **74** 9972–9979 (2000).
664 https://doi.org/10.1128/jvi.74.21.9972-9979.2000.
665 [15] Hamaguchi, M., Yoshida, T., Nishikawa, K., Naruse, H., Nagai, Y. Transcriptive complex of
666 Newcastle disease virus: I. Both L and P proteins are required to constitute an active complex.
667 Virology. **128** 105–117 (1983). https://doi.org/https://doi.org/10.1016/0042-6822(83)90322-
668 7.
669 [16] Horikami, S.M., Curran, J., Kolakofsky, D., Moyer, S.A. Complexes of Sendai virus NP-P and P-L
670 proteins are required for defective interfering particle genome replication in vitro. J. Virol. **66**
671 4901–4908 (1992). https://doi.org/10.1128/jvi.66.8.4901-4908.1992.
672 [17] Bloyet, L.-M. The Nucleocapsid of Paramyxoviruses: Structure and Function of an
673 Encapsidated Template. Viruses. **13** (2021). https://doi.org/10.3390/v13122465.
674 [18] Battisti, A.J. et al. Structure and assembly of a paramyxovirus matrix protein. Proc. Natl. Acad.
675 Sci. **109** 13996–14000 (2012). https://doi.org/10.1073/pnas.1210275109.
676 [19] Ke, Z. et al. Promotion of virus assembly and organization by the measles virus matrix protein.
677 Nat. Commun. **9** 1736 (2018). https://doi.org/10.1038/s41467-018-04058-2.
678 [20] Finch, J.T., Gibbs, A.J. Observations on the Structure of the Nucleocapsids of some
679 Paramyxoviruses. J. Gen. Virol. **6** 141–150 (1970).
680 https://doi.org/https://doi.org/10.1099/0022-1317-6-1-141.
681 [21] Egelman, E.H., Wu, S.S., Amrein, M., Portner, A., Murti, G. The Sendai virus nucleocapsid
682 exists in at least four different helical states. J. Virol. **63** 2233–2243 (1989).
683 https://doi.org/10.1128/JVI.63.5.2233-2243.1989.
684 [22] Bhella, D., Ralph, A., Murphy, L.B., Yeo, R.P. Significant differences in nucleocapsid
685 morphology within the Paramyxoviridae. J. Gen. Virol. **83** 1831–1839 (2002).
686 https://doi.org/https://doi.org/10.1099/0022-1317-83-8-1831.
687 [23] Schoehn, G. et al. The 12 Å structure of trypsin-treated measles virus N-RNA. J. Mol. Biol. **339**

688 301–312 (2004). https://doi.org/10.1016/j.jmb.2004.03.073.
689 [24] Bhella, D., Ralph, A., Yeo, R.P. Conformational flexibility in recombinant measles virus
690 nucleocapsids visualised by cryo-negative stain electron microscopy and real-space helical
691 reconstruction. J. Mol. Biol. **340** 319–331 (2004). https://doi.org/10.1016/j.jmb.2004.05.015.
692 [25] Tawar, R.G. et al. Crystal Structure of a Nucleocapsid-Like Nucleoprotein-RNA Complex of
693 Respiratory Syncytial Virus. Science (80-.). **326** 1279–1283 (2009).
694 https://doi.org/10.1126/science.1177634.
695 [26] Bakker, S.E. et al. The respiratory syncytial virus nucleoprotein-RNA complex forms a left-
696 handed helical nucleocapsid. J. Gen. Virol. **94** 1734–1738 (2013).
697 https://doi.org/10.1099/vir.0.053025-0.
698 [27] Cox, R. et al. Structural studies on the authentic mumps virus nucleocapsid showing uncoiling
699 by the phosphoprotein. Proc. Natl. Acad. Sci. U. S. A. **111** 15208–15213 (2014).
700 https://doi.org/10.1073/pnas.1413268111.
701 [28] Gutsche, I. et al. Near-atomic cryo-EM structure of the helical measles virus nucleocapsid.
702 Science (80-.). **348** 704–707 (2015). https://doi.org/10.1126/science.aaa5137.
703 [29] Desfosses, A. et al. Assembly and cryo-EM structures of RNA-specific measles virus
704 nucleocapsids provide mechanistic insight into paramyxoviral replication. Proc. Natl. Acad.
705 Sci. **116** 4256–4264 (2019). https://doi.org/10.1073/pnas.1816417116.
706 [30] Iseni, F. et al. Chemical modification of nucleotide bases and mRNA editing depend on
707 hexamer or nucleoprotein phase in Sendai virus nucleocapsids. RNA. **8** 1056–1067 (2002).
708 https://doi.org/10.1017/S1355838202029977.
709 [31] Zinzula, L. et al. Cryo-EM structure of the cetacean morbillivirus nucleoprotein-RNA complex.
710 J. Struct. Biol. **213** 107750 (2021). https://doi.org/https://doi.org/10.1016/j.jsb.2021.107750.
711 [32] Ker, D.S., Jenkins, H.T., Greive, S.J., Antson, A.A. CryoEM structure of the Nipah virus
712 nucleocapsid assembly. PLoS Pathog. **17** 1–8 (2021).
713 https://doi.org/10.1371/journal.ppat.1009740.
714 [33] Green, T.J., Zhang, X., Wartz, G.W., Luo, M. Structure of the vesicular stomatitis virus
715 nucleoprotein-RNA complex. Science (80-.). **313** 357–360 (2006).
716 https://doi.org/10.1126/science.1126953.
717 [34] Albertini, A.A.V. et al. Crystal structure of the rabies virus nucleoprotein-RNA complex.
718 Science (80-.). **313** 360–363 (2006). https://doi.org/10.1126/science.1125280.
719 [35] Alayyoubi, M., Leser, G.P., Kors, C.A., Lamb, R.A. Structure of the paramyxovirus
720 parainfluenza virus 5 nucleoprotein-RNA complex. Proc. Natl. Acad. Sci. U. S. A. **112** E1792–
721 E1799 (2015). https://doi.org/10.1073/pnas.1503941112.

722 [36] Conley, M.J. et al. Helical ordering of envelope-associated proteins and glycoproteins in
723 respiratory syncytial virus. EMBO J. **41** e109728 (2022).
724 https://doi.org/10.15252/embj.2021109728.
725 [37] Song, X. et al. Self-capping of nucleoprotein filaments protects the newcastle disease virus
726 genome. Elife. **8** 1–19 (2019). https://doi.org/10.7554/eLife.45057.
727 [38] Zhang, N. et al. Structure and assembly of double-headed Sendai virus nucleocapsids.
728 Commun. Biol. **4** 1–10 (2021). https://doi.org/10.1038/s42003-021-02027-y.
729 [39] Hyatt, A.D., Zaki, S.R., Goldsmith, C.S., Wise, T.G., Hengstberger, S.G. Ultrastructure of Hendra
730 virus and Nipah virus within cultured cells and host animals. Microbes Infect. **3** 297–306
731 (2001). https://doi.org/10.1016/S1286-4579(01)01383-1.
732 [40] Pearce, L.A. et al. Structural characterization by transmission electron microscopy and
733 immunoreactivity of recombinant Hendra virus nucleocapsid protein expressed and purified
734 from Escherichia coli. Protein Expr. Purif. **116** 19–29 (2015).
735 https://doi.org/10.1016/j.pep.2015.07.008.
736 [41] Thompson, R.F., Iadanza, M.G., Hesketh, E.L., Rawson, S., Ranson, N.A. Collection, pre-
737 processing and on-the-fly analysis of data for high-resolution, single-particle cryo-electron
738 microscopy. Nat. Protoc. **14** 100–118 (2019). https://doi.org/10.1038/s41596-018-0084-8.
739 [42] Scheres, S.H.W. RELION: Implementation of a Bayesian approach to cryo-EM structure
740 determination. J. Struct. Biol. **180** 519–530 (2012).
741 https://doi.org/https://doi.org/10.1016/j.jsb.2012.09.006.
742 [43] Krissinel, E., Henrick, K. Inference of macromolecular assemblies from crystalline state. J. Mol.
743 Biol. **372** 774–797 (2007). https://doi.org/10.1016/j.jmb.2007.05.022.
744 [44] Yabukarski, F. et al. Structure of Nipah virus unassembled nucleoprotein in complex with its
745 viral chaperone. Nat. Struct. Mol. Biol. **21** 754–759 (2014).
746 https://doi.org/10.1038/nsmb.2868.
747 [45] Curran, J., Marq, J.B., Kolakofsky, D. An N-terminal domain of the Sendai paramyxovirus P
748 protein acts as a chaperone for the NP protein during the nascent chain assembly step of
749 genome replication. J. Virol. **69** 849–855 (1995). https://doi.org/10.1128/JVI.69.2.849-
750 855.1995.
751 [46] Spehner, D., Drillien, R., Howley, P.M. The assembly of the measles virus nucleoprotein into
752 nucleocapsid-like particles is modulated by the phosphoprotein. Virology. **232** 260–268
753 (1997). https://doi.org/10.1006/viro.1997.8568.
754 [47] Mavrakis, M. et al. Rabies virus chaperone: identification of the phosphoprotein peptide that
755 keeps nucleoprotein soluble and free from non-specific RNA. Virology. **349** 422–429 (2006).

756 https://doi.org/10.1016/j.virol.2006.01.030.
757 [48] Plemper, R.K., Lamb, R.A. Paramyxoviridae: The Viruses and Their Replication, in: Fields Virol.
758 Vol. 1 Emerg. Viruses, 7th Ed, Wolters Kluwer, Philadelphia, 2021: pp. 504–549.
759 [49] Milles, S. et al. Self-Assembly of Measles Virus Nucleocapsid-like Particles: Kinetics and RNA
760 Sequence Dependence. Angew. Chem. Int. Ed. Engl. **55** 9356–9360 (2016).
761 https://doi.org/10.1002/anie.201602619.
762 [50] Blumberg, B.M., Giorgi, C., Kolakofsky, D. N protein of vesicular stomatitis virus selectively
763 encapsidates leader RNA in vitro. Cell. **32** 559–567 (1983). https://doi.org/10.1016/0092-
764 8674(83)90475-0.
765 [51] Gao, Y. et al. In vitro trackable assembly of RNA-specific nucleocapsids of the respiratory
766 syncytial virus. J. Biol. Chem. **295** 883–895 (2020).
767 https://doi.org/10.1074/jbc.RA119.011602.
768 [52] International Committee on Taxonomy of Viruses (ICTV) Taxonomy. Taxonomy. (2023).
769 https://ictv.global/taxonomy/.
770 [53] Harcourt, B.H. et al. Molecular characterization of Nipah virus, a newly emergent
771 paramyxovirus. Virology. **271** 334–349 (2000). https://doi.org/10.1006/viro.2000.0340.
772 [54] International Committee on Taxonomy of Viruses (ICTV) Taxonomy. Taxonomy. (2020).
773 https://ictv.global/taxonomy/.
774 [55] Lee, B., Broder, C.C., Wang, L.-F. Henipaviruses: Hendra and Nipah Viruses, in: Fields Virol.
775 Vol. 1 Emerg. Viruses, 7th Ed, Wolters Kluwer, Philadelphia, 2021: pp. 559–590.
776 [56] Lee, S.-H. et al. Discovery and Genetic Characterization of Novel Paramyxoviruses Related to
777 the Genus Henipavirus in Crocidura Species in the Republic of Korea. Viruses. **13** (2021).
778 https://doi.org/10.3390/v13102020.
779 [57] Madera, S. et al. Discovery and Genomic Characterization of a Novel Henipavirus, Angavokely
780 Virus, from Fruit Bats in Madagascar. J. Virol. e0092122 (2022).
781 https://doi.org/10.1128/jvi.00921-22.
782 [58] Zhang, X.-A. et al. A Zoonotic Henipavirus in Febrile Patients in China. N. Engl. J. Med. **387**
783 470–472 (2022). https://doi.org/10.1056/NEJMc2202705.
784 [59] Annand, E.J. et al. Novel Hendra Virus Variant Detected by Sentinel Surveillance of Horses in
785 Australia. Emerg. Infect. Dis. **28** 693–704 (2022). https://doi.org/10.3201/eid2803.211245.
786 [60] Gonnin, L. et al. Structural landscape of the respiratory syncytial virus nucleocapsids. Nat.
787 Commun. **14** 5732 (2023). https://doi.org/10.1038/s41467-023-41439-8.
788 [61] Noton, S.L., Deflubé, L.R., Tremaglio, C.Z., Fearns, R. The respiratory syncytial virus
789 polymerase has multiple RNA synthesis activities at the promoter. PLoS Pathog. **8** e1002980

790 (2012). https://doi.org/10.1371/journal.ppat.1002980.
791 [62] Tremaglio, C.Z., Noton, S.L., Deflubé, L.R., Fearns, R. Respiratory syncytial virus polymerase
792 can initiate transcription from position 3 of the leader promoter. J. Virol. **87** 3196–3207
793 (2013). https://doi.org/10.1128/JVI.02862-12.
794 [63] Braun, M.R. et al. RNA elongation by respiratory syncytial virus polymerase is calibrated by
795 conserved region V. PLoS Pathog. **13** e1006803 (2017).
796 https://doi.org/10.1371/journal.ppat.1006803.
797 [64] Rager, M., Vongpunsawad, S., Duprex, W.P., Cattaneo, R. Polyploid measles virus with
798 hexameric genome length. EMBO J. **21** 2364–2372 (2002).
799 https://doi.org/10.1093/emboj/21.10.2364.
800 [65] Loney, C., Mottet-Osman, G., Roux, L., Bhella, D. Paramyxovirus ultrastructure and genome
801 packaging: cryo-electron tomography of sendai virus. J. Virol. **83** 8191–8197 (2009).
802 https://doi.org/10.1128/JVI.00693-09.
803 [66] Beniac, D.R. et al. The organisation of Ebola virus reveals a capacity for extensive, modular
804 polyploidy. PLoS One. **7** e29608 (2012). https://doi.org/10.1371/journal.pone.0029608.
805 [67] Goff, P.H., Gao, Q., Palese, P. A majority of infectious Newcastle disease virus particles
806 contain a single genome, while a minority contain multiple genomes. J. Virol. **86** 10852–
807 10856 (2012). https://doi.org/10.1128/JVI.01298-12.
808 [68] Iseni, F. et al. Sendai virus trailer RNA binds TIAR, a cellular protein involved in virus-induced
809 apoptosis. EMBO J. **21** 5141–5150 (2002). https://doi.org/10.1093/emboj/cdf513.
810 [69] Hanley, L.L. et al. Roles of the respiratory syncytial virus trailer region: effects of mutations on
811 genome production and stress granule formation. Virology. **406** 241–252 (2010).
812 https://doi.org/10.1016/j.virol.2010.07.006.
813 [70] Rincheval, V. et al. Functional organization of cytoplasmic inclusion bodies in cells infected by
814 respiratory syncytial virus. Nat. Commun. **8** 563 (2017). https://doi.org/10.1038/s41467-017-
815 00655-9.
816 [71] Roden, C., Gladfelter, A.S. RNA contributions to the form and function of biomolecular
817 condensates. Nat. Rev. Mol. Cell Biol. **22** 183–195 (2021). https://doi.org/10.1038/s41580-
818 020-0264-6.
819 [72] Zhang, X. et al. Molecular mechanisms of stress-induced reactivation in mumps virus
820 condensates. BioRxiv. 2021.07.10.451879 (2022).
821 https://doi.org/10.1101/2021.07.10.451879.
822 [73] Cattaneo, R., Rebmann, G., Baczko, K., ter Meulen, V., Billeter, M.A. Altered ratios of measles
823 virus transcripts in diseased human brains. Virology. **160** 523–526 (1987).

824 https://doi.org/10.1016/0042-6822(87)90031-6.
825 [74] Bloyet, L.-M. et al. Modulation of Re-initiation of Measles Virus Transcription at Intergenic
826 Regions by PXD to NTAIL Binding Strength. PLOS Pathog. **12** e1006058 (2016).
827 https://doi.org/10.1371/journal.ppat.1006058.
828 [75] Zheng, S.Q. et al. MotionCor2: anisotropic correction of beam-induced motion for improved
829 cryo-electron microscopy. Nat. Methods. **14** 331–332 (2017).
830 https://doi.org/10.1038/nmeth.4193.
831 [76] Zhang, K. Gctf: Real-time CTF determination and correction. J. Struct. Biol. **193** 1–12 (2016).
832 https://doi.org/10.1016/j.jsb.2015.11.003.
833 [77] Pettersen, E.F. et al. UCSF Chimera - A visualization system for exploratory research and
834 analysis. J. Comput. Chem. **25** 1605–1612 (2004). https://doi.org/10.1002/jcc.20084.
835 [78] Goddard, T.D. et al. UCSF ChimeraX: Meeting modern challenges in visualization and analysis.
836 Protein Sci. **27** 14–25 (2018). https://doi.org/10.1002/pro.3235.
837 [79] Pettersen, E.F. et al. UCSF ChimeraX: Structure visualization for researchers, educators, and
838 developers. Protein Sci. **30** 70–82 (2021). https://doi.org/10.1002/pro.3943.
839 [80] Waterhouse, A. et al. SWISS-MODEL: Homology modelling of protein structures and
840 complexes. Nucleic Acids Res. **46** W296–W303 (2018). https://doi.org/10.1093/nar/gky427.
841 [81] Cowtan, K. The Buccaneer software for automated model building. 1. Tracing protein chains.
842 Acta Crystallogr. Sect. D Biol. Crystallogr. **62** 1002–1011 (2006).
843 https://doi.org/10.1107/S0907444906022116.
844 [82] Emsley, P., Cowtan, K. Coot: model-building tools for molecular graphics. Acta Crystallogr. D.
845 Biol. Crystallogr. **60** 2126–2132 (2004). https://doi.org/10.1107/S0907444904019158.
846 [83] Emsley, P., Lohkamp, B., Scott, W.G., Cowtan, K. Features and development of Coot. Acta
847 Crystallogr. Sect. D Biol. Crystallogr. **66** 486–501 (2010).
848 https://doi.org/10.1107/S0907444910007493.
849 [84] Adams, P.D. et al. PHENIX: a comprehensive Python-based system for macromolecular
850 structure solution. Acta Crystallogr. D. Biol. Crystallogr. **66** 213–221 (2010).
851 https://doi.org/10.1107/S0907444909052925.
852 [85] Afonine, P. V. et al. Real-space refinement in PHENIX for cryo-EM and crystallography. Acta
853 Crystallogr. Sect. D Struct. Biol. **74** 531–544 (2018).
854 https://doi.org/10.1107/S2059798318006551.
855 [86] Chen, V.B. et al. MolProbity: all-atom structure validation for macromolecular
856 crystallography. Acta Crystallogr. D. Biol. Crystallogr. **66** 12–21 (2010).
857 https://doi.org/10.1107/S0907444909042073.

[87] Williams, C.J. et al. MolProbity: More and better reference data for improved all-atom structure validation. Protein Sci. **27** 293–315 (2018). https://doi.org/10.1002/pro.3330.

[88] Kyte, J., Doolittle, R.F. A simple method for displaying the hydropathic character of a protein. J. Mol. Biol. **157** 105–132 (1982). https://doi.org/10.1016/0022-2836(82)90515-0.

Acknowledgements

This research has received funding from the European Union Horizon 2020 research and innovation programme, under the Marie Skłodowska-Curie Actions grant agreement no. 721367 (HONOURs). The FEI Titan Krios microscopes were funded by the University of Leeds (UoL ABSL award) and The Wellcome Trust (108466/Z/15/Z). The FEI Vitrobot was funded by The Wellcome Trust, grant 218785/Z/19/Z. All *E. coli* strains were produced in house by Susan Matthews. Valuable suggestions during cryoEM data processing and model building were given by Dr. David Nicholson and Dr. David Klebl.

Author Contributions

TCP, JNB, and TAE conceptualised the work. JNB and TAE were responsible for primary supervision of the investigation. TCP carried out the investigation. DPM assisted in cryoEM data collection. JBRW and MJB provided critical input in data processing. TCP visualised the data and prepared the manuscript. JNB, TAE, and NAR provided valuable feedback on the investigation and manuscript. JNB and TAE acquired funding for the work.

Additional Information

Competing Interests

The authors declare no competing interests.

885 **Figure Legends**

886 **Figure 1. Structure of the HeV N protein-RNA double-ring assembly.** The cryoEM map (**a-b**),
887 resolved to 3.5 Å resolution, and reconstructed HeV N multimer (**c**) and protomer (**d**) were coloured
888 according to HeV N protein domains (**e**). Views of the map showing a complete double-ring assembly
889 (**a**) or single tetradecameric ring (**b**) are shown aligned to the corresponding view of the
890 reconstructed multimer (**c**). The multimeric assembly reveals that the top of each tetradecameric
891 ring consists of the C-terminal arm (Ct-arm; gold) which lies on top of the globular C-terminal
892 domain (CTD; green) (**a**). The globular N-terminal domains (NTDs; orange) intercalate to form a
893 dimer of tetradecamers (right panels). The N-terminal arm (Nt-arm; blue) lies completely within the
894 double-ring central cavity (**b**) where its loop region jumps over the NTD and its alpha-helical coil
895 interfaces with the CTD. **d**) A focused view of a single HeV N protomer from the double-ring
896 assembly shows the bound RNA (sticks; coloured by element). **e**) Schematic, to-scale linear
897 representation of the HeV N protein domain architecture indicating the Ncore and Ntail regions. The
898 Ncore consists of the NTD and CTD, each of which are flanked by a flexible arm; the Nt-arm and the
899 Ct-arm. The intrinsically disordered Ntail region was not resolved in the cryoEM map nor modelled in
900 the reconstruction.

901

902 **Figure 2. HeV N protein double-ring surface values.** The presence of a strongly negatively charged
903 patch (Asp3, Asp6, Glu7) is indicated within the context of a HeV N protomer (**a**) or a tetradecameric
904 ring (**b**). The protomer or ring of interest is coloured according to electrostatic surface potentials for
905 negative (red, -) and positive (blue, +) residues or uncoloured (white) for neutral residues. HeV N
906 protomers or tetradecameric ring adjacent to the protomer or ring of interest, respectively, are
907 transparent.

908

909 **Figure 3. HeV N_{i+1} Nt arm residues Phe11 and Leu31 are buried in conserved pockets on the**
910 **neighbouring N_i globular domains. a**) The N_{i+1} Nt-arm residue Phe11 (red) sits within a conserved
911 hydrophobic pocket consisting of the neighbouring N_i protomer CTD residues Phe267, Phe268, and
912 Tyr301 (grey sticks). Surface colours are mapped to Kyte-Doolittle hydrophobicity scale [88] from
913 most hydrophilic (green, ζ) to most hydrophobic (gold, ϕ). The RNA is represented as a dark grey
914 ribbon. **b**) The N_{i+1} Nt-arm residue Leu31 (red) engages in electrostatic interactions with the
915 neighbouring N_i protomer NTD residues Asn43, Arg48, Tyr80, Glu82, Met158, Leu161, Val162, and
916 Val165 (grey sticks). Electrostatic surface potentials are coloured for negative (red, -) and positive
917 (blue, +) residues or uncoloured (white) for neutral residues.

918

919 **Figure 4. The HeV double-ring assembly forms elbow interactions bridging non-neighbouring**
920 **protomers.** Three N protomers in the assembled ring, showing the N_i (pale blue), N_{i+1} (coral), and N_{i-1}
921 (green) protomers, centred on the elbow interaction between the N_{i+1} Nt-arm and the N_{i-1} Ct-arm. **a**)
922 A surface render of three adjacent N protomers within the assembled ring with their Nt-arm (Nt),
923 CTD, and Ct-arm (Ct) indicated. **b-c**) A ribbon visualisation of three N protomers. Protomers N_{i+1} and
924 N_{i-1} are coloured white and the N_i is coloured pale blue. Putative interacting residues are coloured
925 coral and green and presented as sticks. **b**) Residues putatively involved in the elbow interactions are
926 shown as sticks and indicated. **c**) The cryoEM double-ring density map is shown as a transparent
927 overlay.
928
929 **Figure 5. The HeV double-ring assembly intercalation zone is poorly resolved.** A ribbon visualisation
930 of a dimer of N pentamers. N protomers are coloured white with loops belonging to the intercalation
931 zone coloured per protomer. Putative interacting residues are presented as sticks. **a**) An overview of
932 the dimer of pentamers assembly showing the intercalation zone. **b-c**) The intercalation zone
933 centred around the N_i protomer (lime) of the top ring, showing the N_{i+1} (pink) protomer as well as
934 the bottom ring protomers N_i (n_i; gold), N_{i-1} (n_{i-1}; purple), and N_{i+1} (n_{i-1}; coral). **b**) Residues putatively
935 involved in the intercalation interactions are shown as sticks and indicated. Italicised residues are
936 stubbed and modelled as alanines. **c**) The cryoEM double-ring density map is shown as a transparent
937 overlay revealing areas of poor density.
938
939 **Figure 6. The HeV N protein binds RNA through electrostatic and hydrophobic interactions. a**)
940 Three N protomers within the assembled ring with the N_i protomer as a surface render and the
941 neighbouring N_{i+1} and N_{i-1} protomers as ribbons. The N protein domains are individually coloured;
942 the Nt-arm in blue, the NTD in orange, the CTD in green, and the Ct-arm in gold. The 18-mer RNA
943 chain is visualised as sticks and follows heteroatom colouring. **b-c**) Two different close ups of the
944 RNA binding cleft centred on the N_i protomer. N proteins are visualised as ribbons and the RNA
945 chain as sticks. Helices and loops containing putative RNA interacting residues are coloured for the N_i
946 (NTD; gold, CTD; green), the N_{i+1} (purple), and the N_{i-1} (coral). RNA bases in each hexamer are
947 numbered 1 to 6 on a per-N protomer basis from the 3'- to the 5'-end. **d**) A topological schematic of
948 the RNA-interacting residues centred around the Ni protomer and the corresponding RNA hexamer.
949 RNA base stack orientations are shown and bases in each hexamer are numbered 1 to 6 from the 3'-
950 to the 5'-end. Putative protein-RNA interactions are indicated for electrostatic interactions (blue
951 dashed line) and hydrophobic interactions (green dashed arc). Residues belonging to neighbouring N
952 protomers are bounded by a dashed box.

953

954 **Figure 7. Neighbouring HeV N protomers form an in-base cavity. a**) A trimer of N protomers as
955 surface renders and individually coloured; N_i (light blue), N_{i+1} (coral), and N_{i-1} (green). Protomer
956 domains (NTD, CTD, Nt-arm, and Ct-arm) are indicated. The trimer was sliced between two
957 neighbouring protomers (1) and down the frontal face (2) to reveal the RNA binding cleft (orange
958 dashed area) and in-base cavities (white dashed area). The RNA chain has been removed for clarity.
959 **b**) An N protein dimer centred on the in-base cavity. Helices and loops that form the in-base cavity
960 are coloured for the N_i (light blue) and the N_{i+1} (coral). Putative RNA-base interacting residue side
961 chains are visualised as sticks and indicated. The N_i Ct-arm has been removed for clarity. RNA bases
962 in each hexamer are numbered 1 to 6 on a per-N protomer basis from the 3'- to the 5'-end.
963

964 **Figure 8. Comparison of the HeV N protein double-ring assembly to N protein assemblies from**
965 **related viruses. a-b**) Structural alignment of the HeV N protein model and two NiV N protein models.
966 Models are presented as ribbons, with the HeV structure in green and the NiV structures in red. **a**)
967 Alignment of the HeV N protein with the crystal structure of NiV N protein (PDB: 4CO6) with a global,
968 pruned RMSD of 0.783 Å. The * indicates a 15.5 Å shift in position of the His369 Cα. The HeV N
969 protomer-bound RNA hexamer was removed and the Nt- and Ct-arms were truncated to resemble
970 the truncated apo-NiV N protein. The NiV P protein domain present in the crystal structure was also
971 removed for clarity. **b**) Alignment of the HeV N protein with the helical cryoEM structure of NiV N
972 protein (PDB: 7NT5) with a global, pruned RMSD of 0.756 Å. **c-f**) The structures of the multimeric N-
973 protein assemblies of (**c**) SeV (PDB: 6M7D, EMD-30129), (**d**) NDV (PDB: 6JC3, EMD-9793, (**e**) NiV
974 (PDB: 7NT5, EMD-12581), and (**f**) HeV (this study) are presented with the N_{i+1} (red) and N_{i-1} (green)
975 protomers as ribbons and the bound RNA as black sticks inside their respective EM density maps
976 (transparent grey). The Ni protomer models are not visualised for clarity but the density map is
977 retained. The N_{i+1} utmost N-terminal residue resolved in each model is indicated by an asterisk,
978 corresponding to SeV Gly3 (**c**), NDV Met1 (**d**), NiV Ile4 (**e**), and HeV Met1 (**f**) which are distended
979 away from the N_{i-1} Ct-arm loop for SeV, NDV, and NiV (**c-e**) but not for HeV (**f**). The HeV N-terminal
980 purification tag (hexahistidine-SUMO) was proteolytically removed prior to cryoEM grid preparation.
981 The N-terminal hexahistidine-tag (SeV and NDV) or N-terminal hexahistidine-3C-tag (NiV) was
982 retained but not resolved.

Figure 1

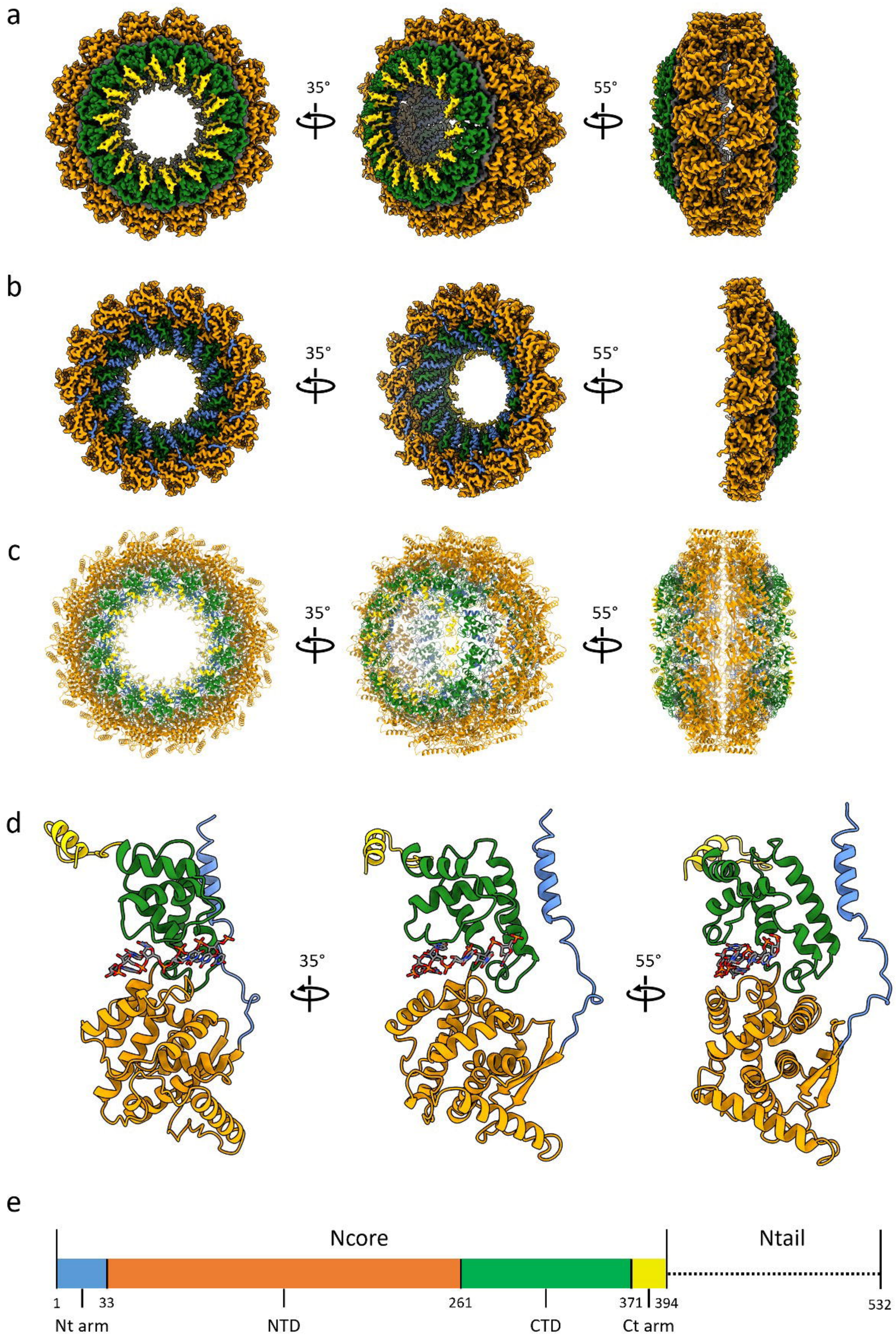
a
35°
55°
b
35°
55°
c
35°
55°
d
35°
55°
e
Ncore
Ntail
1
33
261
371
394
532
Nt arm
NTD
CTD
Ct arm

Figure 2

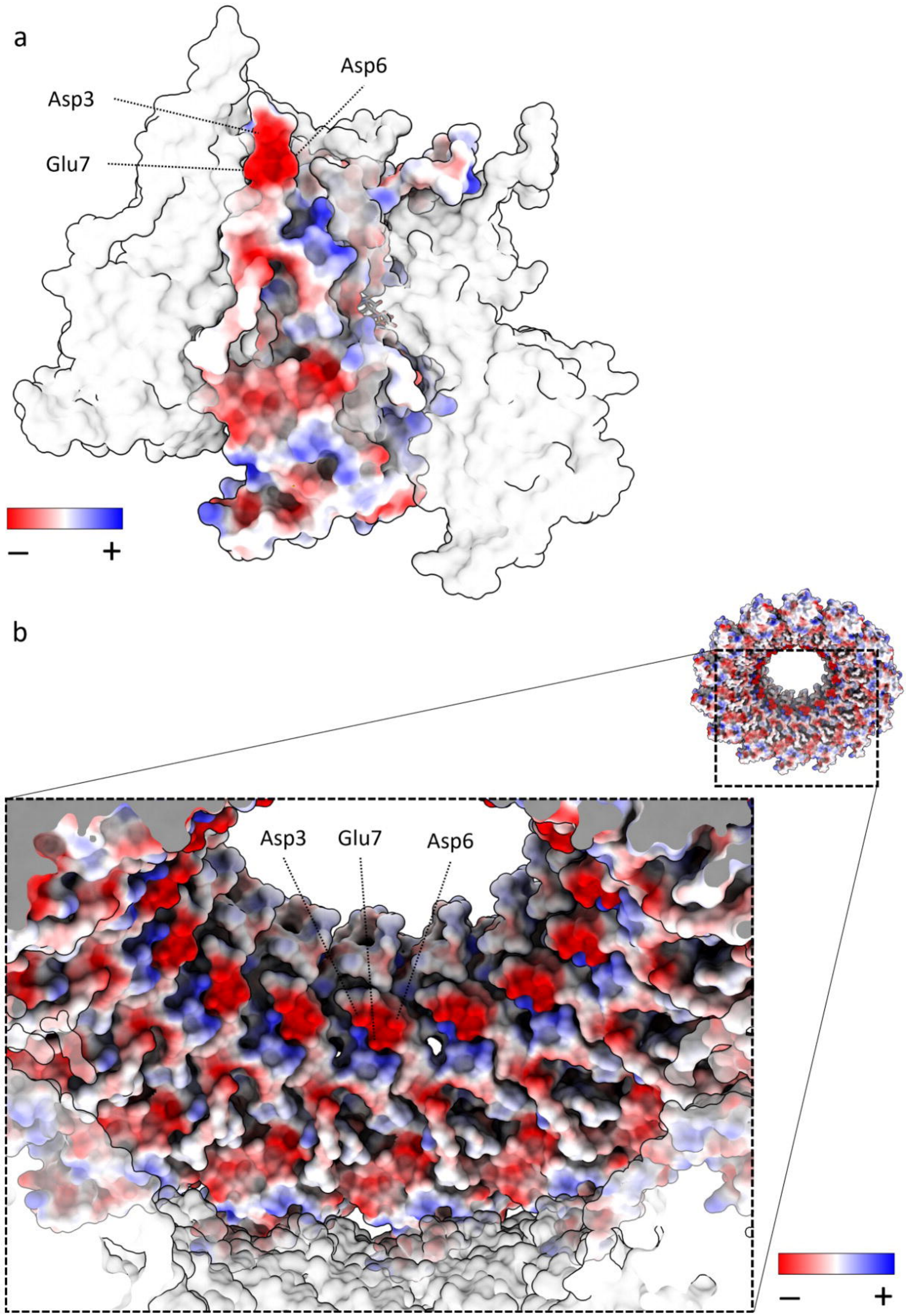

Figure 3

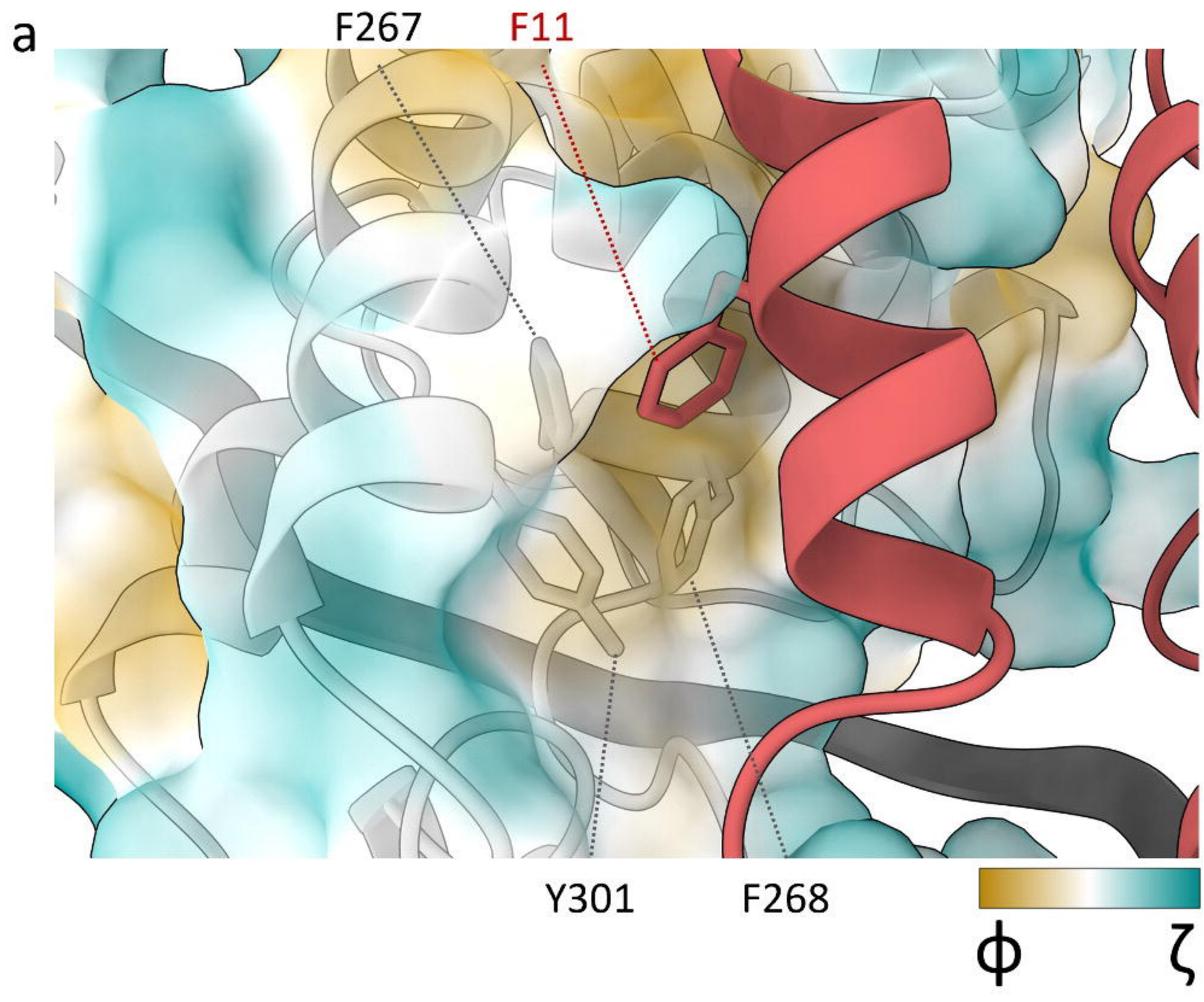
a
F267
F11
Y301
F268
ϕ
ζ

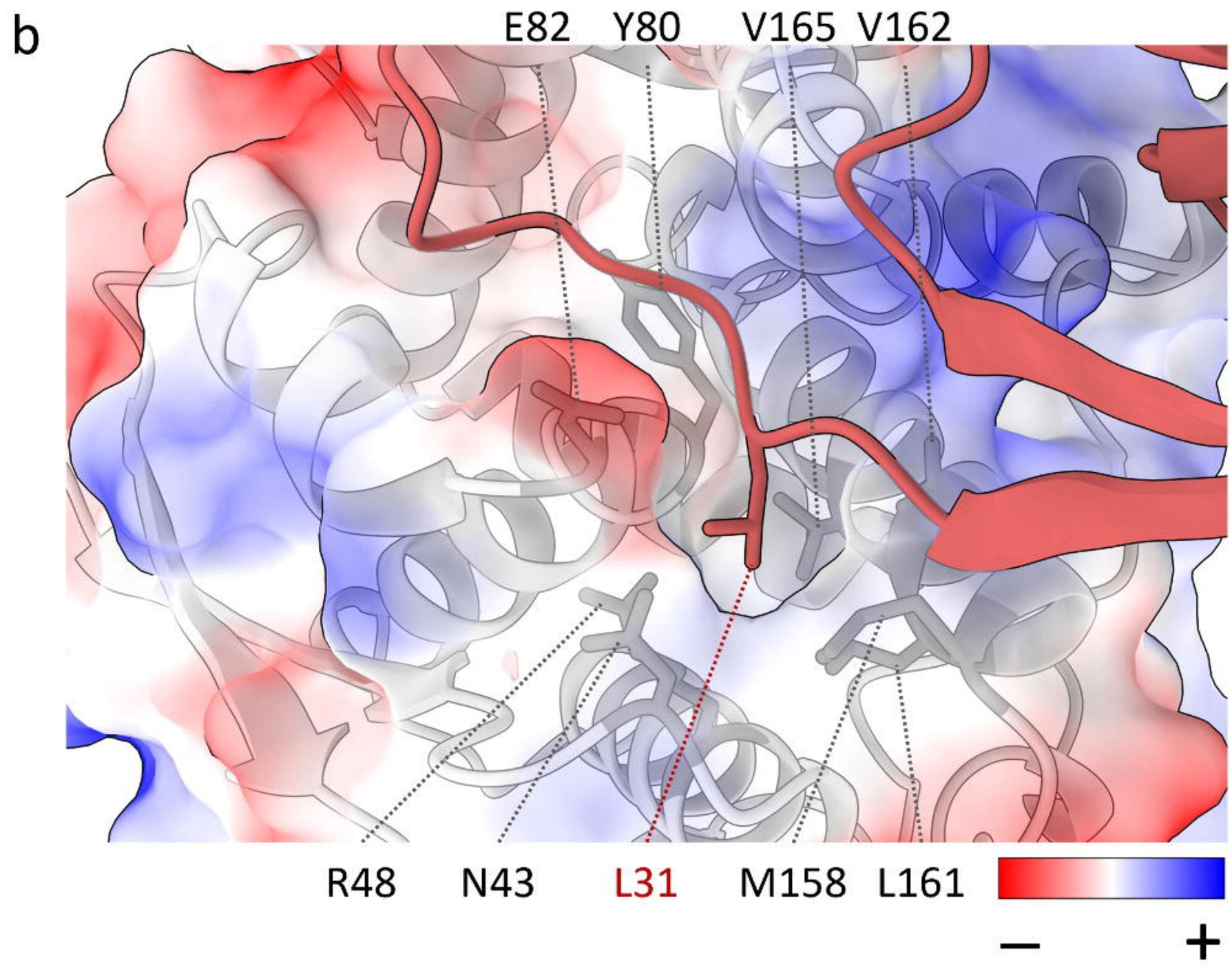
b
E82
Y80
V165
V162
R48
N43
L31
M158
L161
−
+

Figure 4

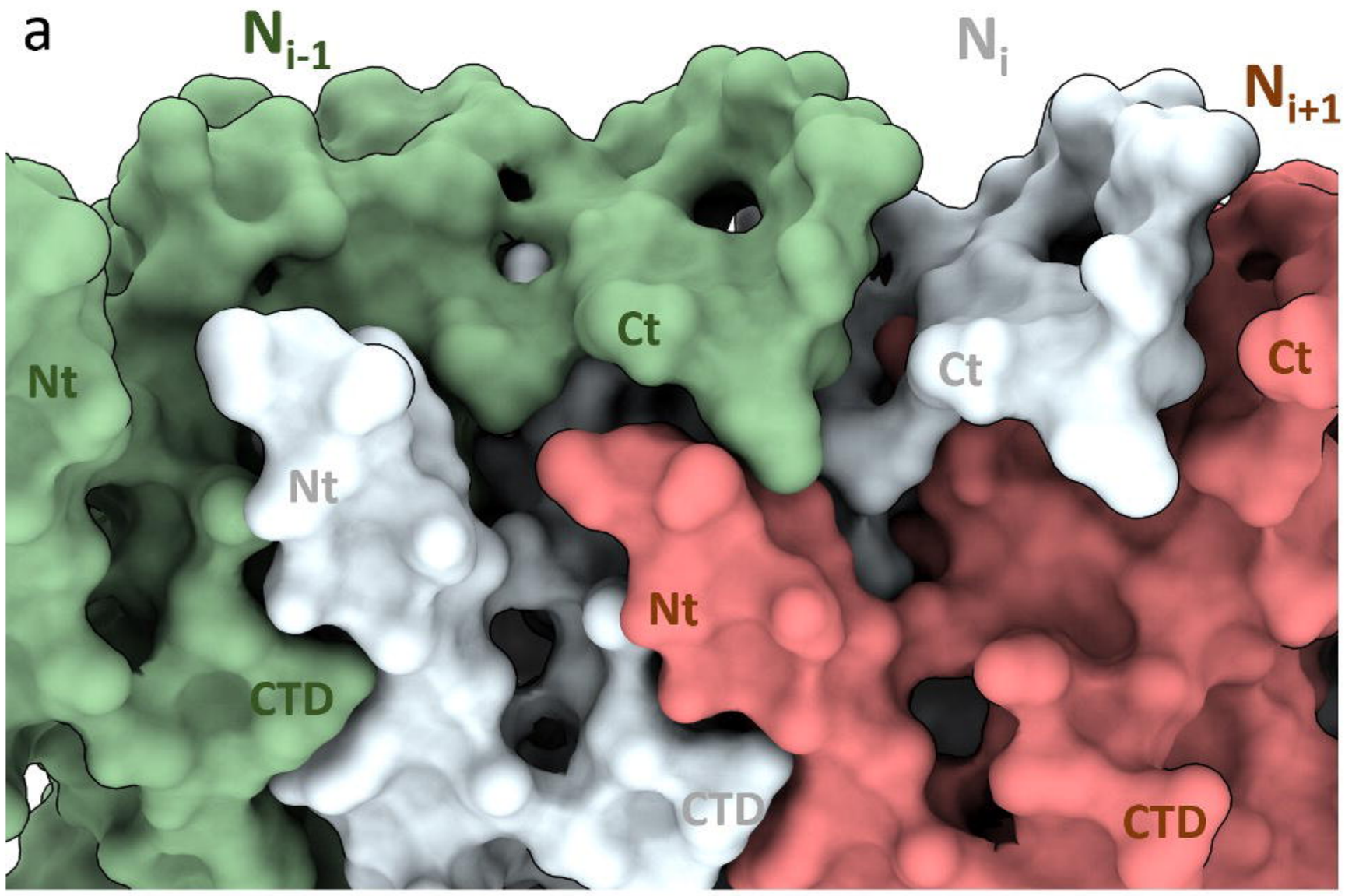
a
N_{i-1}
N_i
N_{i+1}
Nt
Ct
Nt
Ct
Ct
Nt
CTD
CTD
CTD

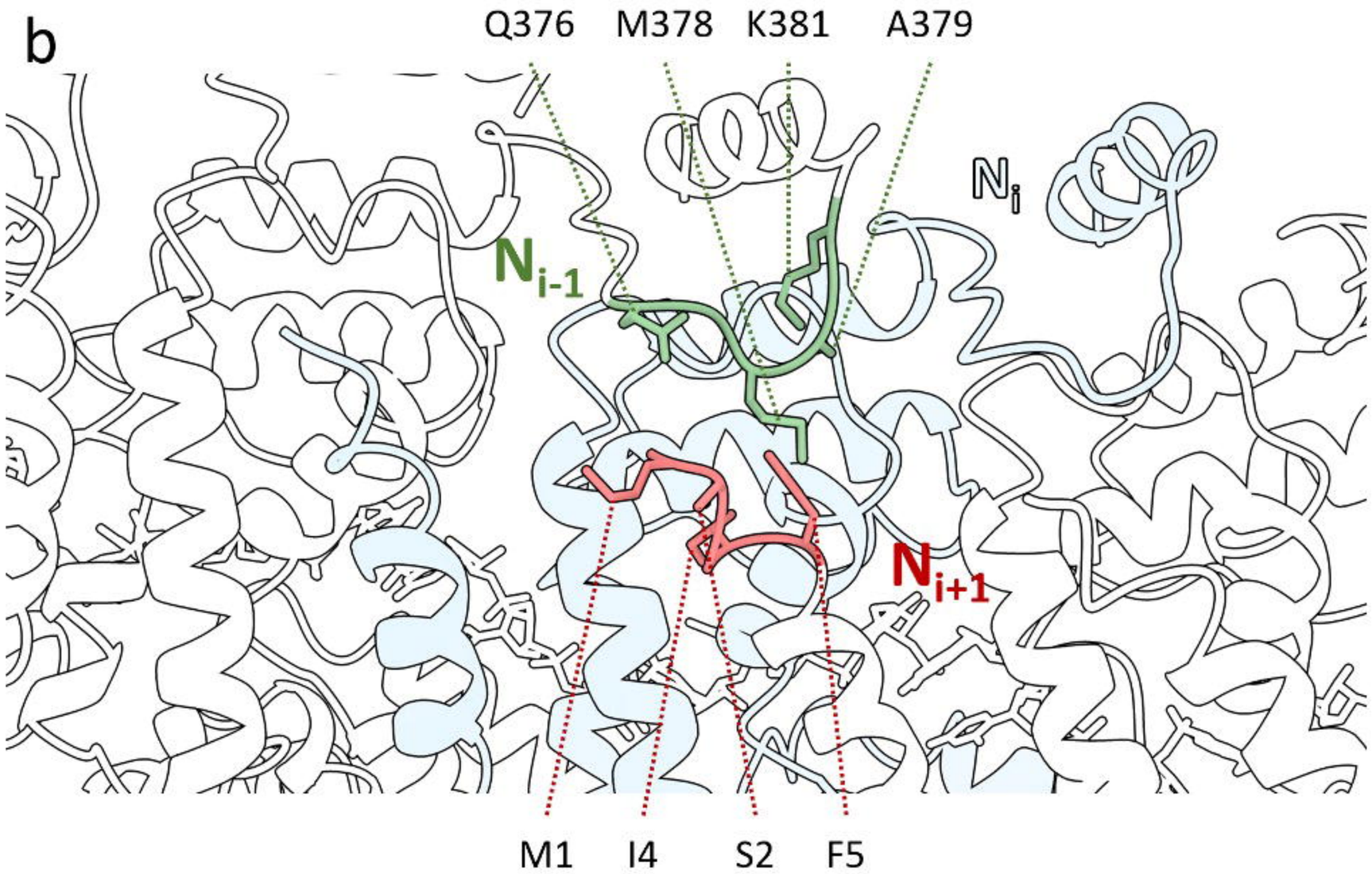
b
Q376
M378
K381
A379
N_i
N_{i-1}
N_{i+1}
M1
I4
S2
F5

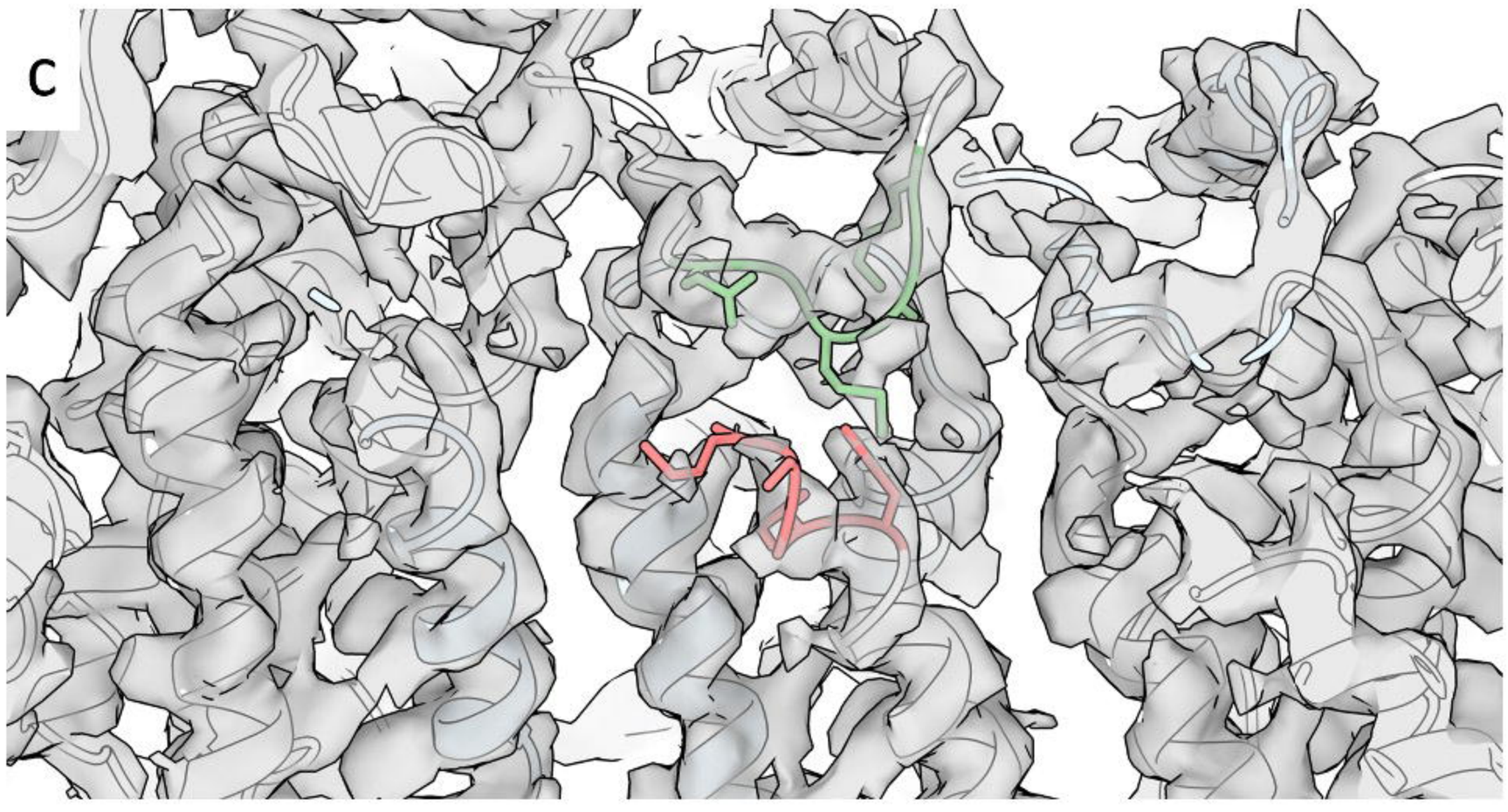
c

Figure 5

a

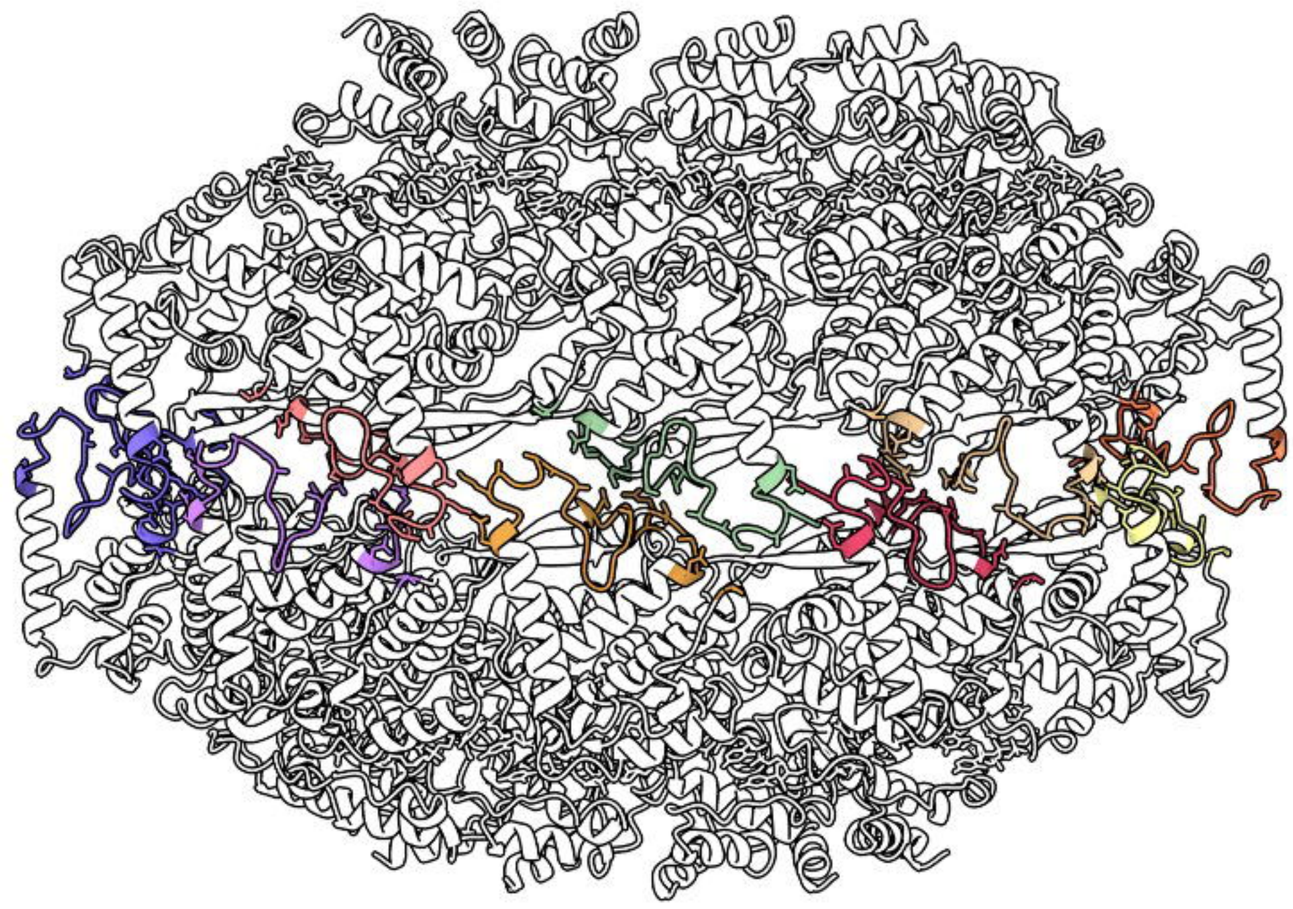

b

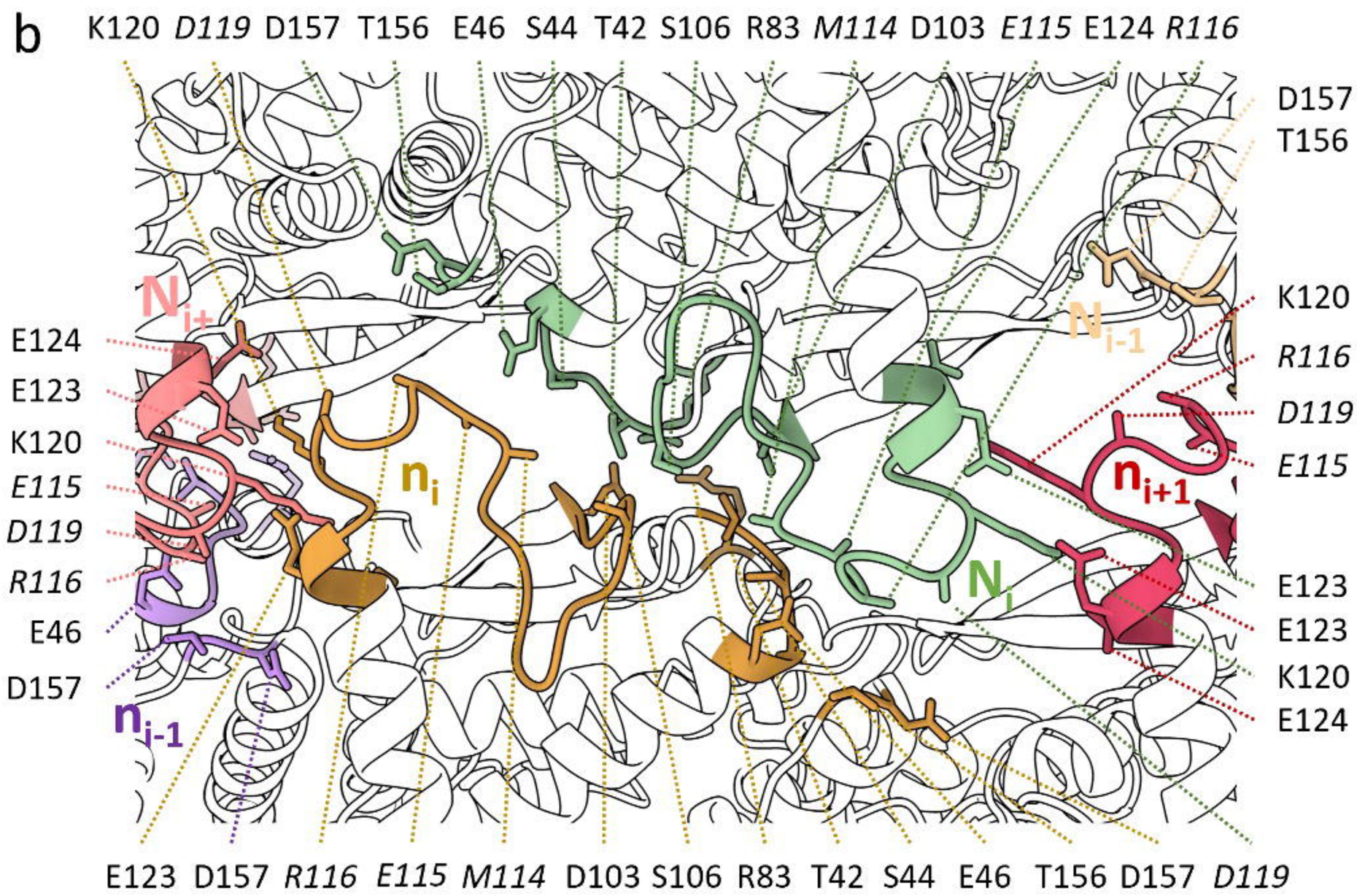
K120 D119 D157 T156 E46 S44 T42 S106 R83 M114 D103 E115 E124 R116
E124
E123
K120
E115
D119
R116
E46
D157
D157
T156
K120
R116
D119
E115
E123
E123
K120
E124
N_{i+}
N_{i-1}
n_i
n_{i+1}
N_i
n_{i-1}
E123 D157 R116 E115 M114 D103 S106 R83 T42 S44 E46 T156 D157 D119

c

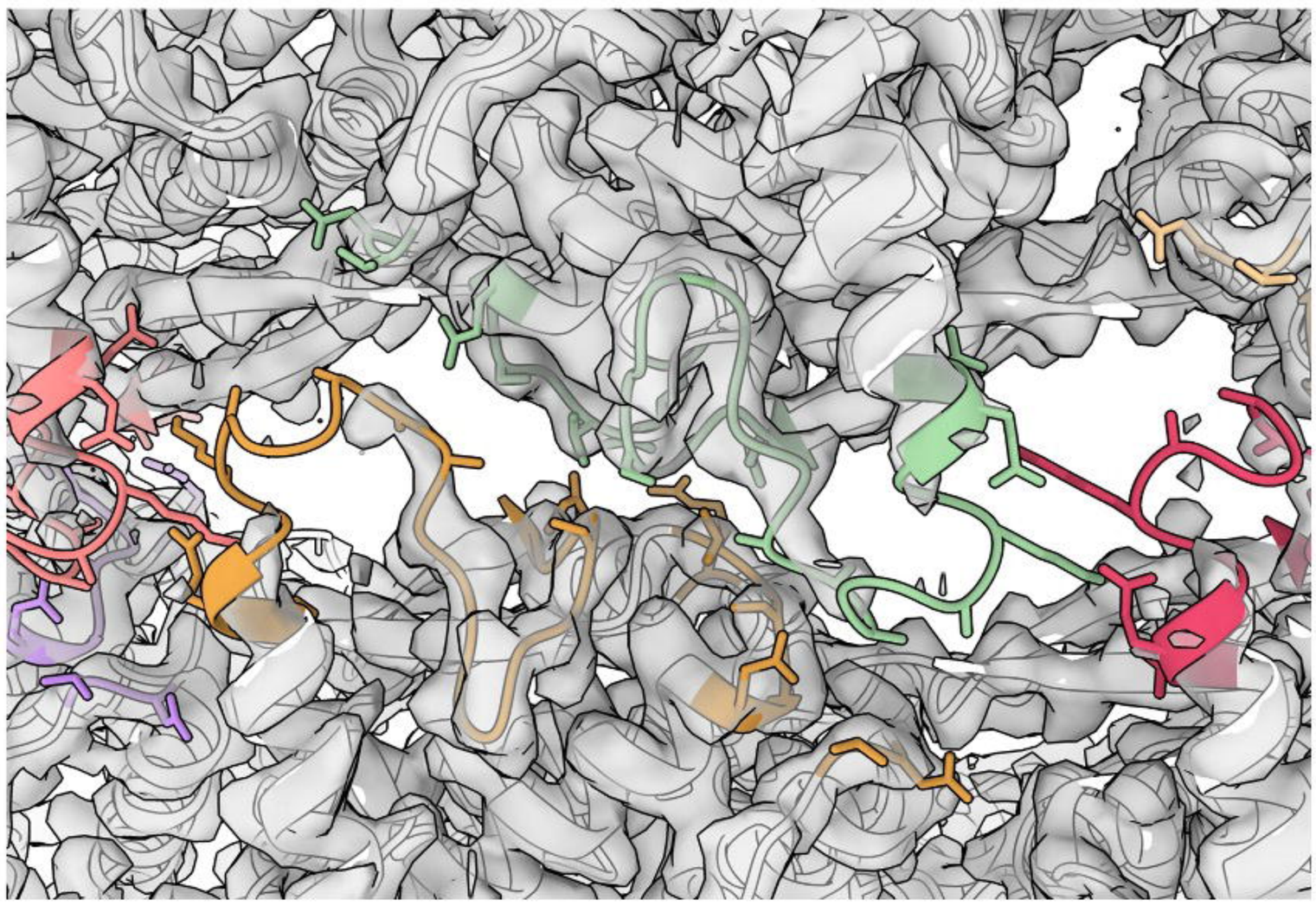

Figure 6

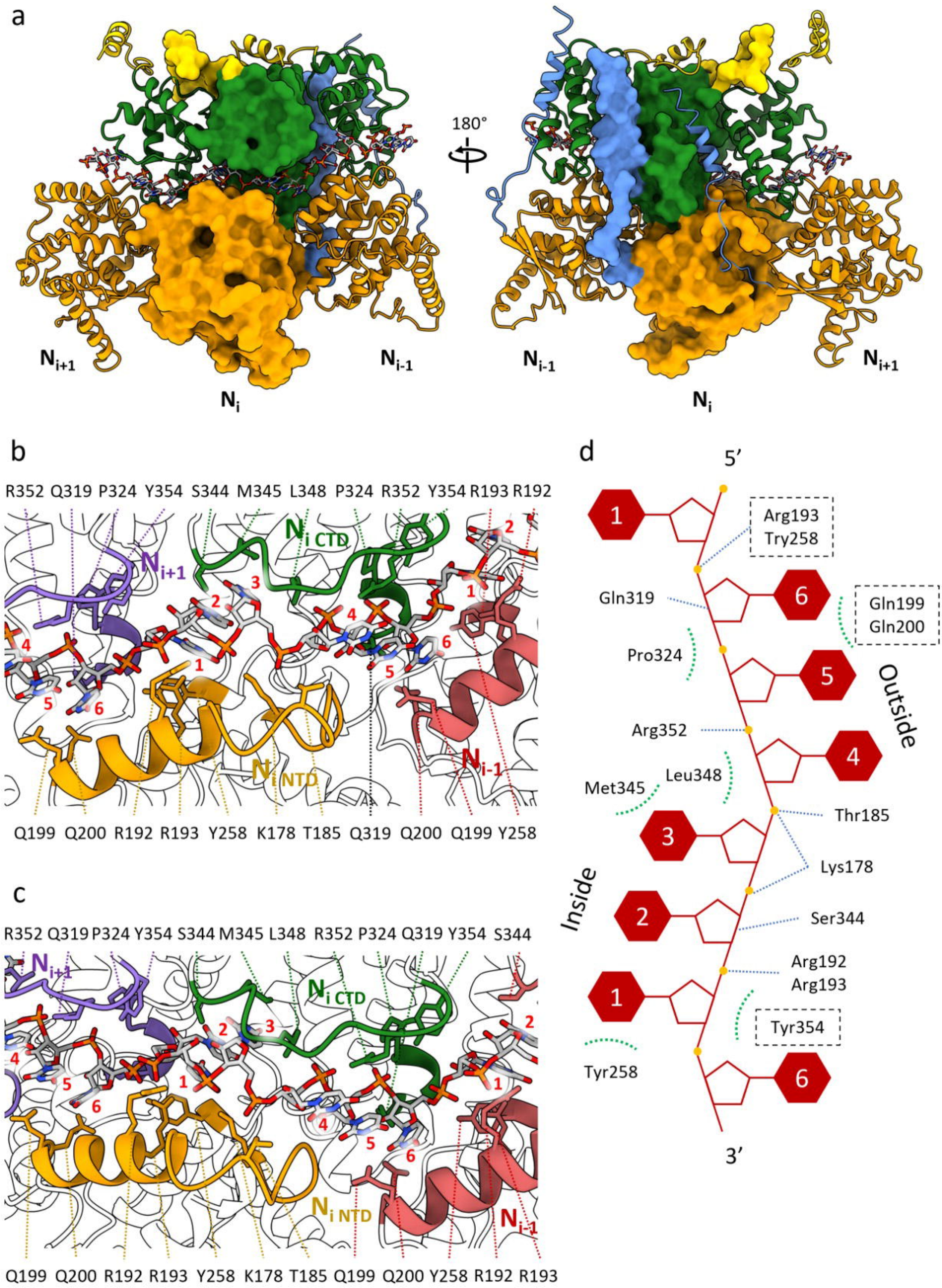
a
180°
N_{i+1}
N_i
N_{i-1}
N_{i-1}
N_i
N_{i+1}
b
R352 Q319 P324 Y354 S344 M345 L348 P324 R352 Y354 R193 R192
N_{i+1}
$N_{i\ CTD}$
$N_{i\ NTD}$
N_{i-1}
Q199 Q200 R192 R193 Y258 K178 T185 Q319 Q200 Q199 Y258
c
R352 Q319 P324 Y354 S344 M345 L348 R352 P324 Q319 Y354 S344
N_{i+1}
$N_{i\ CTD}$
$N_{i\ NTD}$
N_{i-1}
Q199 Q200 R192 R193 Y258 K178 T185 Q199 Q200 Y258 R192 R193
d
5'
3'
Arg193
Try258
Gln319
Gln199
Gln200
Pro324
Outside
Arg352
Leu348
Met345
Thr185
Lys178
Inside
Ser344
Arg192
Arg193
Tyr354
Tyr258

Figure 7

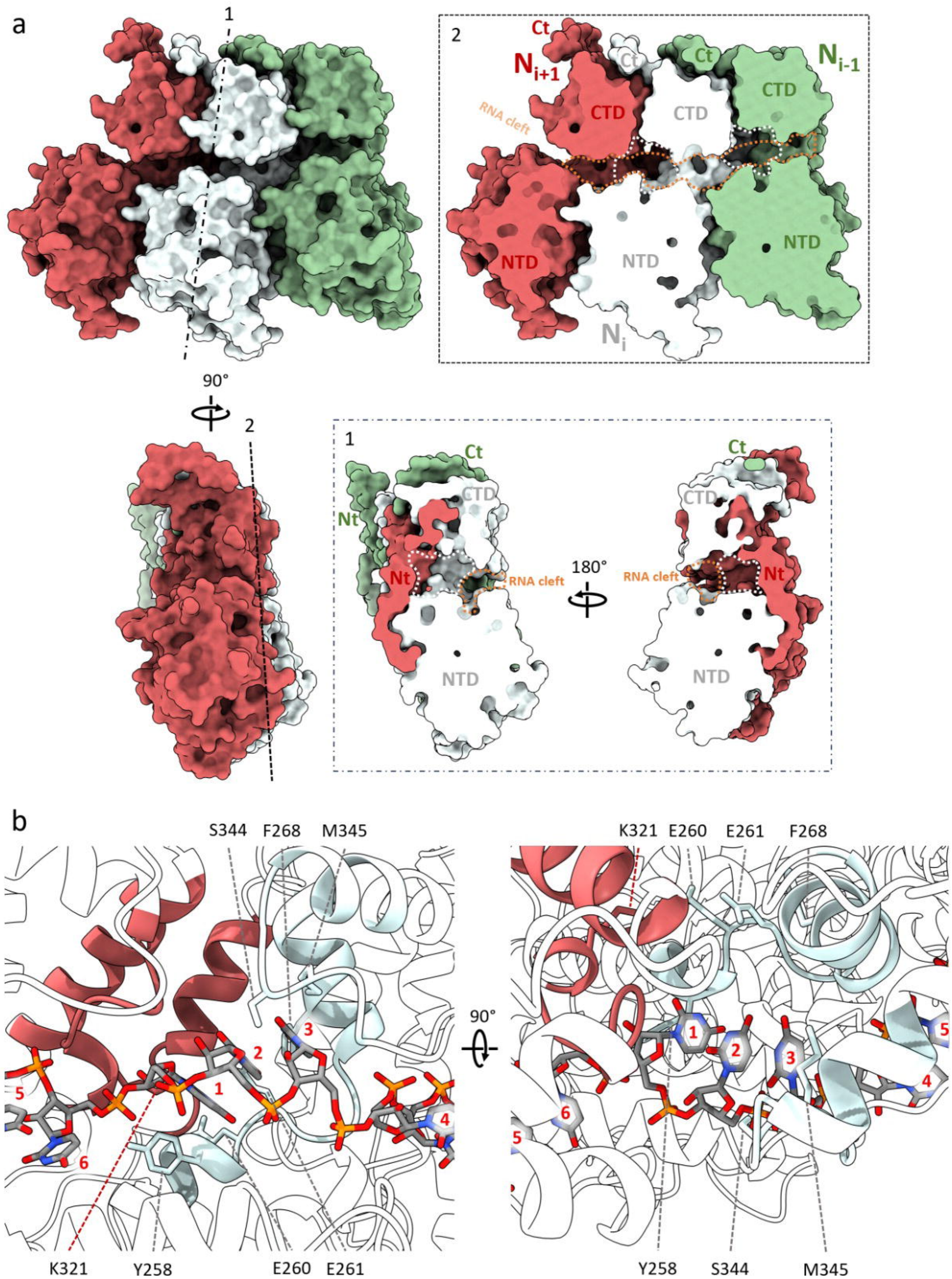
a
1
2
Ct
N_{i+1}
Ct
Ct
N_{i-1}
CTD
CTD
CTD
RNA cleft
NTD
NTD
NTD
N_i
90°
2
1
Ct
CTD
Nt
Nt
RNA cleft
NTD
180°
Ct
CTD
RNA cleft
Nt
NTD
b
S344
F268
M345
K321
E260
E261
F268
90°
K321
Y258
E260
E261
Y258
S344
M345

Figure 8

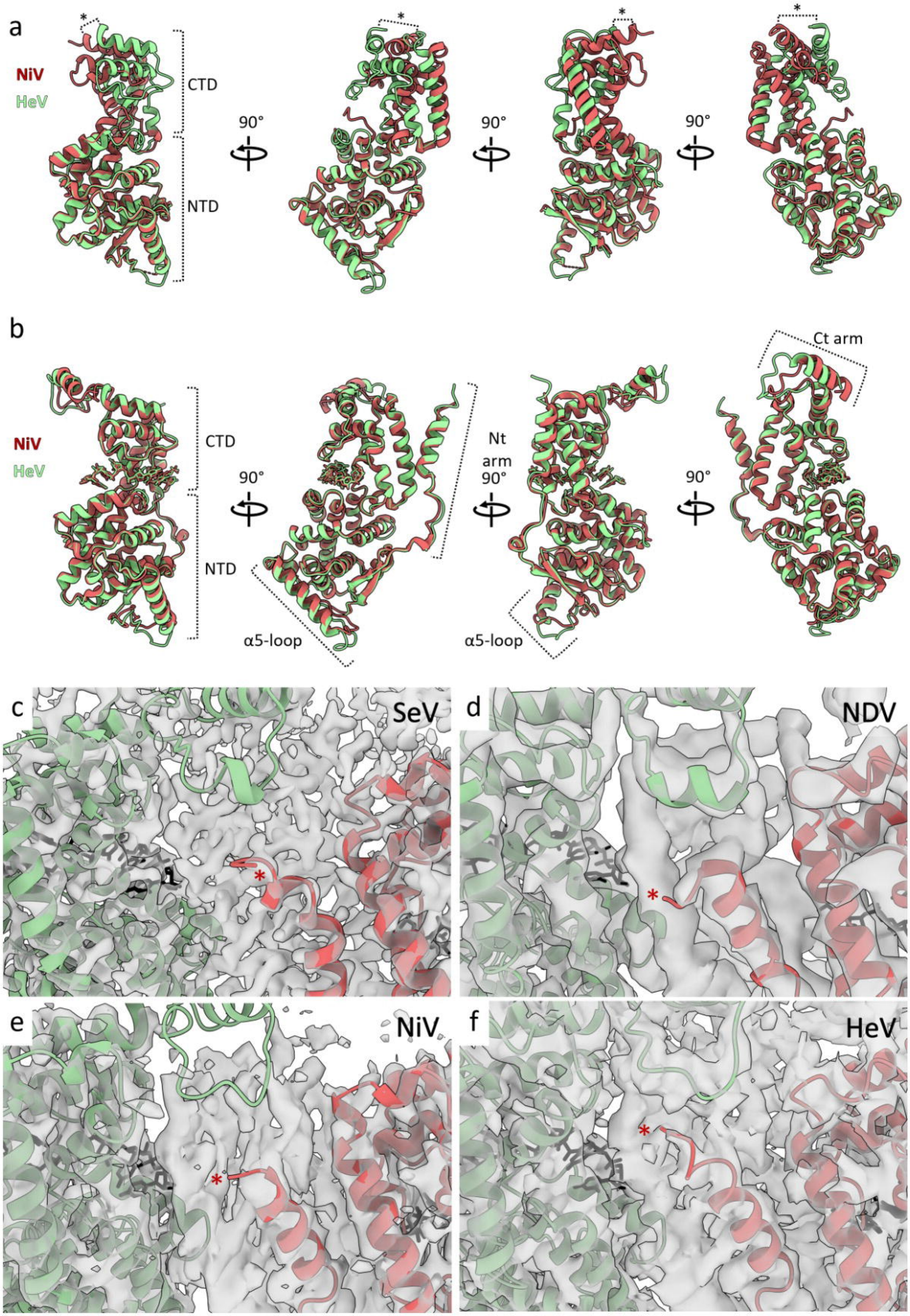
a
NiV
HeV
CTD
NTD
90°
90°
90°
b
NiV
HeV
CTD
NTD
90°
α5-loop
Nt
arm
90°
α5-loop
90°
Ct arm
c
SeV
d
NDV
e
NiV
f
HeV